Supporting Information

The Role of Bulk and Interfacial Morphology in Charge Generation, Recombination, and Extraction in Non-Fullerene Acceptor Organic Solar Cells

Akchheta Karki, Joachim Vollbrecht, Alexander J. Gillett, Steven Shuyong Xiao, Yali Yang, Zhengxing Peng, Nora Schopp, Alana L. Dixon, Sangcheol Yoon, Max Schrock, Harald Ade, G. N. Manjunatha Reddy, Richard H. Friend*, Thuc-Quyen Nguyen**

Prof. T.-Q. N., Dr. A. K., Dr. J. V., N. S., A. L. D., M. S.
Center for Polymers and Organic Solids, University of California Santa Barbara (UCSB), Santa Barbara, California 93106, USA
E-mail: quyen@chem.ucsb.edu

Prof. R. H. F., Dr. A. J. G.
Optoelectronics Group Cavendish Laboratory
University of Cambridge, J. J. Thomson Avenue
Cambridge CB3 0HE, UK
E-mail: rhf10@cam.ac.uk

Dr. S. S. Xiao, Dr. Y. Y.
1-Material Inc, 2290 Chemin St-François
Dorval, Quebec, H9P 1K2, Canada

Prof. H. A., Z. P.
Department of Physics and Organic and Carbon Electronics Laboratories (ORaCEL)
North Carolina State University
Raleigh, North Carolina 27695, USA

Dr. G. N. M. R.
Department of Chemistry, University of Lille, CNRS, Centrale Lille Institut, Univ. Artois, UMR 8181−UCCS− Unité de Catalyse et Chimie du Solide, F-59000, Lille, France
E-mail: gnm.reddy@univ-lille.fr

Keywords: bulk and interfacial morphology, charge generation, charge recombination, charge extraction, D:A electronic coupling

Table of contents **Page**

1. Experimental section

Materials and synthesis. Different batches of the PM6 polymers and Y6 NFA were synthesized by 1-material inc. **Fig. S1** below depicts the synthetic pathway to the PM6 donor polymer. All reagents were purchased from commercial sources and were used without further purification unless noted otherwise. $Pd(PPh_3)_4$ was purchased from Strem Chemicals, anhydrous toluene was purchased from Sigma-Aldrich. 1M_IT5259(CAS#1514905-25-9; 1,1'-[4,8-bis[5-(2-ethylhexyl)-4-fluoro-2-thienyl]benzo[1,2-*b*:4,5-*b*']dithiophene-2,6-diyl]bis[1,1,1-trimethylstannane; purity 99+%, NMR shown in **Fig. S2**) and 1M_IT9780 (CAS#1415929-78-0; 1,3-bis(5-bromo-2-thienyl)-5,7-bis(2-ethylhexyl4*H*,8*H*-Benzo[1,2-*c*:4,5-*c*']dithiophene-4,8-dione); purity 99+%, NMR shown in **Fig. S3**) are commercially available from 1-Material Inc.

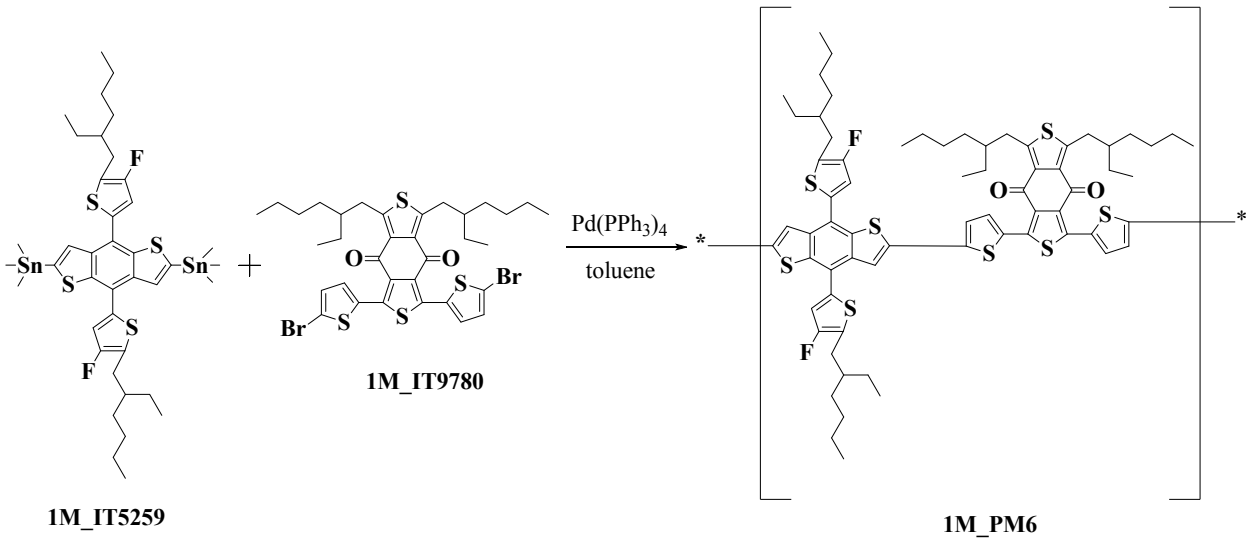

Fig. S1 Schematic of synthesis pathway to PM6 polymer

A four-necked 250 ml flask equipped with a mechanic stirrer, an argon inlet, a condenser caped with an argon outlet, and a thermometer, was thoroughly dried by a torch and cooled to room temperature under continuous flow of argon. Into this reaction flask, 60 ml of anhydrous toluene, 2.82 g of 1M_IT5259 (3.0 mmol), 2.30 g of 1M_IT9780 (3.0 mmol), 151 mg of $Pd(PPh_3)_4$ (0.13 mmol) were added. The reaction mixture was heated using a heating mantel and stirred at 110 °C for 24 h, and subsequentially quenched by 2-(tributylstannyl)thiophene and bromobenzene. Then, the quenched reaction mixture was cooled to room temperature. While vigorously stirring, the cooled polymer solution was dripped into a solvent mixture containing 600 ml of methanol and 600 ml of acetone. The polymer product was collected by filtration and dried naturally overnight to yield a dark solid, which is referred as the crude polymer PM6 (CAS# 1802013-83-7; Poly[[4,8-bis[5-(2-ethylhexyl)-4-fluoro-2-thienyl]benzo[1,2-*b*:4,5-*b*']dithiophene-2,6-diyl]-2,5-thiophenediyl[5,7-bis(2-ethylhexyl)-4,8-dioxo-4*H*,8*H*-benzo[1,2-*c*:4,5-*c*']dithiophene-1,3-diyl]-2,5-thiophenediyl]).

PM6 samples tested here are from different polymerization batches and from different after-treatments. A crude polymer of Lot# YY13208 was transferred to a Soxhlet extractor and was subsequentially extracted by acetone (4 h), hexane (17 h) and chloroform (24 h). The chloroform extracted fraction was concentrated and precipitated in acetone to yield the PM6 sample of YY13208CH. Another crude polymer of Lot#YY15258 was extracted by a Soxhlet extractor following the same procedure of YY13208 to give YY15258CH. However, we found the chloroform solution of YY15258CH was gradually becoming reddish, and we suspected some probable degradation. Thus, we took YY1528CH for further after-treatments to yield SX8055A, SX8055B and SX8055C85, as follows. First, we re-labelled the original YY15258CH as SX8055A for comparing with other SX8055 series. Second, we scavenged SX8055A following our patented procedure described in US Patent 6,894,145 to obtained PM6 sample SX8055B. Thirdly, we used a Soxhlet extractor to extract SX8055A again in a solvent sequence of methanol, acetone, a mixture of 85% chloroform and 15% methanol (referred as C85 herein), and finally chloroform. The fraction extracted by C85 was concentrated and precipitated in acetone, filtered and naturally dried to give sample of SX8055C85.

Gel Permeation Chromatography (GPC). Molecular weight of the PM6 polymers was estimated by GPC method; two peaks were observed for most of batches in GPC profiles. One peak was associated with a low molecular weight fraction with an estimated Mn of 2200-2800 g/mol and another peak was associated with a high molecular weight fraction with an estimated Mn of 30000-50000 g/mol. The polydispersity index (PDI) of all polymers were determined to be the same of around 2.2 to ensure a systematic comparison of the samples. The relative fractions of two peaks obtained from the area integrates associated with different peaks are summarized below in **Table S1**.

Table S1. Summary of GPC fractions of the different PM6 batches.

Sample	Peak-1 (low Mw fraction)		Peak-2 (high Mw fraction)	
	Peak area (%)	Estimated Mn (Da)	Peak area (%)	Estimated Mn (Da)
YY13208CH	1	2400	99	43700
SX8055B	7	2600	93	42500
SX8055A	9	2600	91	42100
SX8055C85	52	2200	48	38900

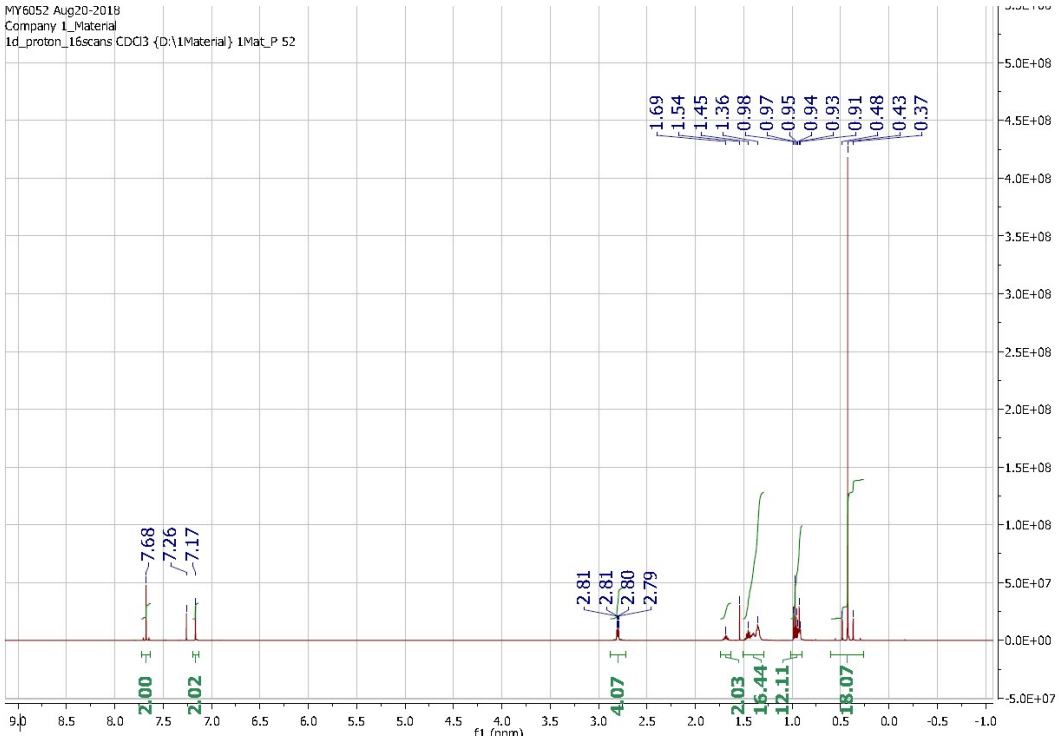

Fig. S2 Solution-state 1D ^{1}H NMR spectrum of 1M_IT5259 in $CDCl_3$.

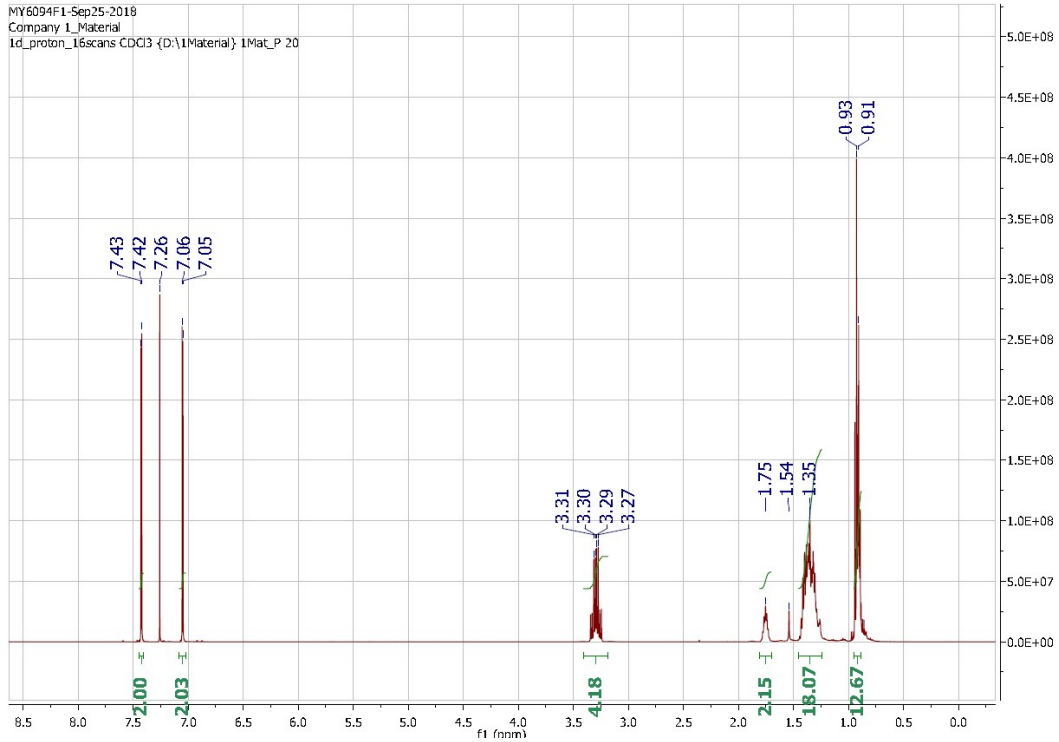

Fig. S3 Solution-state 1D ^{1}H NMR spectrum of 1M_IT9780 in $CDCl_3$.

Device Fabrication: Indium tin oxide (ITO) patterned glass substrates were cleaned by scrubbing with soapy water, followed by sonication in soapy water, deionized (DI) water, acetone, and isopropanol for 20 minutes each. The substrates were dried using compressed nitrogen and placed in an oven overnight at 100 °C. The ITO substrates were treated with UV-ozone for 15 minutes and a layer of poly(3,4-ethylenedioxythiophene): poly(styrenesulfonate) (PEDOT:PSS, Clevios P VP Al 8043) was spin-coated at 3000 rpm for 40 s onto the ITO substrates. The substrates were then annealed in air at 150 °C for 20 minutes. 18 mg/mL of PM6:Y6 blend solutions were prepared with a D:A ratio of 1:1.2 in chloroform with 0.5% v/v 1-chloronaphthanene (CN). The active layers were spin-cast inside a nitrogen glovebox at 4000 rpm and annealed inside the glovebox at 110 ^{0}C for 10 minutes. The substrates were left to cool for 5 minutes and 1 mg/mL PDINO solution dissolved in methanol was spin-coated on top of the active layer. The substrates were then pumped down under vacuum (< 10^{-6} torr), and a 100 nm thick Aluminum electrode was deposited on top of the active layer by thermal evaporation. Devices of neat materials (PM6 or Y6) were prepared using similar solid concentrations as that in the blend solution.

Device Testing: Photovoltaic characteristic measurements were carried out inside the glove box using a high-quality optical fiber to guide the light from the solar simulator equipped with a Keithley 2635A source measurement unit. *J-V* curves were measured under AM 1.5G illumination at 100 mW cm^{-2} for devices with an electrode area of 0.22 cm^2. Every device in the different batches was tested, unless the device did not work at all due to issues with shorting.

External quantum efficiency (EQEPV) measurements: External quantum efficiency (EQE) for all solar cells was measured using a 75 W Xe light source, monochromator, optical chopper (138 Hz), and a lock-in amplifier. Power-density calibration of the EQE characteristics was achieved using a calibrated silicon photodiode from Newport. For the sub-bandgap EQE, higher sensitivity settings were used with a longer time delay between measurement points.

Internal quantum efficiency (IQE) measurements: The total reflectance of the solar cell devices with the configuration: glass/ITO/PEDOT:PSS/Active layer/Ba/Al were measured with an integrating sphere to obtain the total absorption, which was corrected for the parasitic absorption simulated with the transfer matrix model.[1] The active layer optical properties were measured with transmittance and reflectance measurements using an integrating sphere. The optical properties of the other layers were determined from ellipsometry with a Woolam M-2000DI Variable Angle Spectroscopic Ellipsometer, with reflectance and transmission measurements, or taken from the literature.[2,3] The IQE spectra of the devices were calculated by subtracting the parasitic absorption from the total device absorption to obtain the active layer absorption and dividing the EQE spectra by the corresponding fraction of active layer absorption. As described in the literature report,[4] since the experimentally measured total absorption is highly accurate, errors in the resulting active layer absorption are only as small as the errors in the parasitic absorptions.

Electroluminescence and EQE_{EL} Measurements: EL measurements were performed using two setups depending on the wavelength range of interest. For measurements under 1050 nm, a home-made EL spectrometer was used. The EL emission from a sample driven by a Keithley source-measure unit (model 2602A) was collected by a lens system and focused on the entrance slit of a spectrograph (Acton Research SP-500) equipped with a Si charge-coupled detector (Princeton Instruments Pixis:400). The spectra collected by the detector were corrected for the instrument response function. The correction factors were determined by measuring the spectrum of a black body-like light source (Ocean Optics LS-1). For EL measurements in the range 900 - 1700 nm, we utilized a Photon Technology International (PTI) Quantamaster fluorimeter equipped with an Edinburgh Instruments EI-L Ge detector. The excitation monochromator of the fluorimeter was not used, and the EL emission was generated by driving the devices by a Keithley 2602 source-measure unit. An optical chopper (Thorlabs MC2000) was placed in front of the emission monochromator to make use of the fluorimeter's lock-in amplifier-based detection system. The PTI Felix fluorimeter software was used for the data collection and correction of the instrumental artifacts. The efficiency of electroluminescence was obtained by applying a bias from -1 to 2V with a dual-channel Keithley 2602 to the solar cell and placing a silicon or germanium photodiode directly in front of it to collect the emission as a function of applied bias. The current running through the device and the photodiode were simultaneously measured.

Transient Absorption (TA) spectroscopy: TA was performed on either one of two experimental setups. For "visible" region TA (500–950 nm), a Yb amplifier (PHAROS, Light Conversion), operating at 38 kHz and generating 200 fs pulses centred at 1030 nm with an output of 14.5 W was used. The pump pulse was provided by a TOPAS optical parametric amplifier. The probe is provided by a WL supercontinuum generated in a YAG crystal. After passing through the sample, the probe is imaged using a Si photodiode array (Stresing S11490). This setup provided additional flexibility by allowing for broadband spectrum acquisition in one measurement for improved consistency, as well good signal to noise (s/n) in the 750–850 nm region, which is difficult to obtain on the other setups due to large fluctuations in the WL seed around the 800 nm fundamental. The near infrared (NIR) TA was performed on a setup which was powered using a commercially available Ti:sapphire amplifier (Spectra Physics Solstice Ace). The amplifier operates at 1 kHz and generates 100 fs pulses centered at 800 nm with an output of 7 W. For these measurements, a small fraction of the 800 nm fundamental was used as the pump. The probe was provided by a broadband NIR NOPA. To complement the NIR probe wavelengths available, the probe pulses are collected with an InGaAs dual-line array detector (Hamamatsu G11608-512DA), driven and read out by a custom-built board from Stresing Entwicklungsbüro. The probe beam was split into two identical beams by a 50/50 beamsplitter. This allowed for the use of a second reference beam which also passes through the sample but does not interact with the pump. The role of the reference was to correct for any shot-to-shot fluctuations in the probe that would otherwise greatly increase the structured noise in our experiments. Through this arrangement, very small signals with a $\frac{\Delta T}{T} < 10^{-5}$ could be measured.

Capacitance spectroscopy: Capacitance spectroscopy measurements were performed with an impedance analyzer Solartron 1260A in the dark and under 1 sun AM1.5 illumination inside a nitrogen-filled glovebox. The amplitude of the AC signal was 40 mV to ensure a negligible impact on the measured impedance.

Photo-conductive atomic force microscopy (pc-AFM): Photoconductive atomic force microscopy (pc-AFM) measurements were done with an Asylum Research MFP-3D microscope sitting atop an inverted optical microscopy (Olympus, IX71). All measurements were conducted under inert atmosphere. A white light source with a power of 30 W cm^{-2} was used to generate photocurrent morphology which was recorded by an internal preamplifier (Asylum Research ORCA head model). Electrically conductive Chromium/Platinum-coated silicon probes with a spring constant of 0.2 N m^{-1} and resonant frequency of 13 kHz (Budget Sensors) were used. A light spot with 160 μm diameter was focused on the active layer of the device through an inverted optical microscope (Olympus), and the conductive tip was positioned at the center of the light spot.

Grazing incidence wide angle X-ray Scattering (GIWAXS): This measurement was performed at the Advanced Light Source at Lawrence Berkeley National Lab on the 7.3.3 beamline. The sample was scanned for 40 seconds at an incidence angle of 0.12° and a photon energy of 10 keV (λ = 1.24 Å), while under a helium environment to minimize beam damage and reduce air scattering. The width of the incident X-ray beam is about 1 mm, and silver behenate was used to calibrate the lengths in the reciprocal space. A 2D detector (PILATUS 2 M from Dectris) with a sample-to-detector distance of 276.9 mm was used to collect the images. The Nika software package for Igor (by Wavemetrics) and the Igor script WAXStools were used to process the image.

Resonant-Soft X-ray Scattering (R-SoXs): R-SoXS was performed at the beamline 11.0.1.2[5] Advanced Light Source (ALS), Lawrence Berkeley National Laboratory. Samples for R-SoXS measurements were prepared on a PSS modified ITO substrates under the same conditions as those used for device fabrication, and then transferred by floating in water to a 1.5 × 1.5 mm^2, 100 nm thick Si3N4 membrane supported by a 5 × 5 mm, 200 mm thick Si frame (Norcada Inc.). R-SoXS was performed in a transmission geometry with linearly polarized photons under high vacuum (1×10^{-7} torr) and a cooled (–45 °C) CCD (Princeton PI-MTE) was used to capture the soft X-ray scattering 2D maps and PS300 was used for geometry calibration.

Solid-State NMR spectroscopy. Spin-coated PM6 and Y6 materials and different batches of PM6:Y6 blends were extracted from glass substrates and packed into either 1.3 mm or 3.2 mm (outer diameter) zirconia rotors. All fast magic-angle spinning (MAS = 60 KHz) 1D ^{1}H, ^{19}F, and 2D ^{19}F-^{19}F NMR experiments were carried out on a Bruker Avance Neo (21.1 T, Larmor frequencies of ^{1}H and ^{19}F were 900.2 MHz and 845.9 MHz, respectively) spectrometer with 1.3 mm H-X probe head. The nutation frequency of ^{1}H was 100 kHz, corresponding to 90° pulse duration of 2.5 μs. Single-pulse ^{1}H MAS NMR experiments were carried out by co-adding 32

transients with a relaxation delay of 4 s (Fig. S7). 1D ^{19}F MAS NMR spectra of neat materials and blends were acquired using 128 co-added transitions. To probe short and long-range through-space ^{19}F-^{19}F proximities, 2D ^{19}F-^{19}F spin diffusion spectra (Fig. S8) were acquired with 100 ms and 1 s of mixing times, respectively. 2D spectra was acquired using 128 t_1 increments, each with 8 co-added transients, with a rotor-synchronized t_1 increment of 16.66 μs, corresponding to a total experimental time of 6 h for each sample. All 1D $^{13}C\{^1H\}$ cross polarization (CP)-MAS and 2D ^{13}C-^1H heteronuclear correlation (HETCOR) NMR experiments of neat materials and blends were carried out on a Bruker Avance II (9.4 T, Larmor frequencies of ^1H and ^{13}C were respectively 400.1 MHz and 100.6 MHz) spectrometer with 3.2 mm H-X probe. 1D $^{13}C\{^1H\}$ CP-MAS and 2D HETCOR spectra were acquired at ~298 K and at 12.5 kHz MAS. 1D $^{13}C\{^1H\}$ CP-MAS spectra (Fig. S8) were acquired with CP contact times of 0.1 and 4 ms, each by co-adding 2048 transients with a ^1H relaxation delay of 4s, corresponding to an experimental time of 2.4 h. In 2D ^1H-^{13}C HETCOR experiments, the indirect ^1H dimension was acquired with 64 t_1 increments, each with 128 co-added transients, corresponding to a total experimental time of 9 h with a recycle delay of 4 s. The high-power homonuclear decoupling was applied during the acquisition of indirect ^1H dimension using a DUMBO decoupling sequence, and heteronuclear decoupling was applied during the detection of ^{13}C dimension using a SPINAL-64 sequence. 2D time domain spectra were processed with FFT (Fourier Transformation) in both vertical ^1H and horizontal ^{13}C dimensions (Fig. S9-S10). The vertical ^1H dimension spectral width was scaled by 1.6, which corresponds to a DUMBO scaling factor of 0.625. The ^1H and ^{13}C experimental shifts were calibrated with respect to neat TMS using adamantane as an external reference (higher ppm ^{13}C resonance, 35.8 ppm, and the ^1H resonance, 1.85 ppm), and ^{19}F chemical shifts were calibrated to the ^{19}F chemical shift of neat $CFCl_3$ (^{19}F, 0 ppm) as an external reference.

2. Quantifying the voltage losses in these blend systems.

The contributions to the V_{OC} losses in the two blend systems were determined to understand the slight increase in the V_{OC} upon going from the 1% LMWF blend to the 52% LMWF blend. It should be noted that the determination of the CT state energies in these two blends are prone to error, as discussed in some earlier publications[6,7], due to the inability to distinguish the S_1 and CT states unambiguously. Nonetheless, as an estimate, we can confirm that the slight red-shift in the EQE spectra of the low performing blend suggests that the E_{CT} value would be higher for the lower performing blends causing the S_1-CT offset in this blend to be slightly lower (< 0.1 eV) than the higher performing blend (S_1-CT offset ~0.05 eV). Additionally, we find the experimentally measured EQE_{EL} values to be very similar in the two blends indicating that the non-radiative recombination losses in the blends are similar. Therefore, the reduced voltage losses in the low performing blend leading to the slight increase in the V_{OC} is due to a reduction in losses due to the decreased S_1-CT offset. Furthermore, due to the presence of additional bulk traps in the lower performing PM6:Y6 blend system, a systematic comparison between the two blend systems to identify the origins of the non-radiative recombination losses may not be possible within the design rules formulated in the paper to identify origins of non-radiative recombination losses.[8,9] The presence of trap-assisted recombination in the low performing blend will likely further contribute to additional non-radiative recombination losses.

Detailed procedure for obtaining the CT energy:

The E_{CT} was determined by fitting an expression derived from Marcus theory (**Equation S1**) to the tail of the blend EQE_{PV} spectrum.[10,11] However, the CT state is not always pronounced in the low-energy tail of the EQE_{PV} spectra, especially in blends where the energetic offsets between the donor and acceptor are low (i.e., low HOMO-HOMO or LUMO-LUMO offsets)[8,12–14], and it can therefore be difficult to distinguish the energy of the CT state from the donor or acceptor singlet state. It is possible, however, to significantly reduce the degrees of freedom in the fitting by 1) performing a simultaneous fit to both the EQE_{PV} (**Equation S1**) and the EL (**Equation S2**) spectra[6,15–18] using equations derived from Marcus theory, as was first demonstrated by Vandewal *et. al.*[10] and 2) calculating the EQE_{PV} down to 10^{-7} using sensitively measured EL data and the relationship shown in **Equation S3**.[19] The added sensitivity of four orders of magnitude in the measurements allows for the deconvolution of the Gaussian-shaped CT absorption which was previously absent from the sharp absorption tail of the measured EQE data. In fact, a recently published paper[18] has shown that this method significantly lowers errors in the fitting parameters (E_{CT}, λ, f) in low energetic offset systems. In both blend systems, the added sensitivity of up to four orders of magnitude with the calculated EQE_{PV} data (Equation S3) from the reciprocity relationship allows for a better deconvolution of the Gaussian-shaped CT absorption which was previously absent from the sharp absorption tail of the measured EQE_{PV} data. The Marcus fitting used to extrapolate the CT energies are shown in **Fig. S4a,b**. However, it is worth noting that despite the reduction in degrees of freedom in the Marcus fitting, the E_{CT} values obtained here serve only as

an estimate, due to the significant uncertainty that arises in separating the CT state emission and the singlet exciton emission in low energetic offset systems. Therefore, we report the CT energy in the two blends – as has been done in some recently reported papers[6,7,20,21]– with a caveat that the obtained E_{CT} value is an estimate only. Nevertheless, due to the uncertainty in the absolute values of the obtained CT energies, we have also adopted the temperature-dependent V_{OC} method as a second technique to further corroborate the trends of the measured E_{CT} values at room temperature of the two blends **(Fig. S4a,b)**. It has been shown that the extrapolation of temperature-dependent V_{OC} conducted at different light intensities to 0 K corresponds to the E_{CT} value at 0 K.[10] Since the E_{CT} values exhibit some temperature dependence, the values at 0 K will be lower than the values measured at room temperature.[10,22,23] The similar variation in the E_{CT} values between the two blend systems of ~40 meV at both room temperature and 0 K can be used to verify – if not the absolute values – at least the trends in the E_{CT} values measured at room temperature.

The reason why the CT energy is higher is due to a slight blue-shift in the tails of the EQE spectra in the 52% LMWF PM6:Y6 blend. The blue shift in the low performing blend is likely due to the reduction in the conjugation lengths that can shift the tail of the EQE spectra to higher energies (i.e. shift to lower wavelengths). We can expect the 52% LMWF PM6:Y6 blend to have a compromised conjugation compared to the 1% LMWF blend due to the presence of the shorter PM6 polymer chains.

Equations used to obtain the CT energy:

$$EQE_{PV,CT}(E) = \frac{f}{E\sqrt{4\pi\lambda k_B T}} exp\left(\frac{-\left(E_{CT}+\lambda-E\right)^2}{4\lambda k_B T}\right) \quad \text{(S1)}$$

$$EQE_{EL,CT}(E) = E\frac{f}{\sqrt{4\pi\lambda k_B T}} exp\left(\frac{-\left(E_{CT}-\lambda-E\right)^2}{4\lambda k_B T}\right) \quad \text{(S2)}$$

$$EQE_{PV}(E) \propto EL(E)E^{-2}\exp\left(\frac{E}{k_B T}\right) \quad \text{(S3)}$$

Here, k_B is Boltzmann's constant, E is the photon energy, and T is the absolute temperature. The fit parameters are E_{CT}, which is the energy at the point of intersection between CT absorption and emission, λ, which is the reorganization energy, and f, which is a measure of the strength of the donor-acceptor coupling. The solid red and green lines in the Marcus fitting shown in **Figs. S4a,b** shows the calculated blend EQE_{PV} from the EL spectra using **Equation S3** at lower energies, confirming the good match between the measured and experimental EQE_{PV} data.

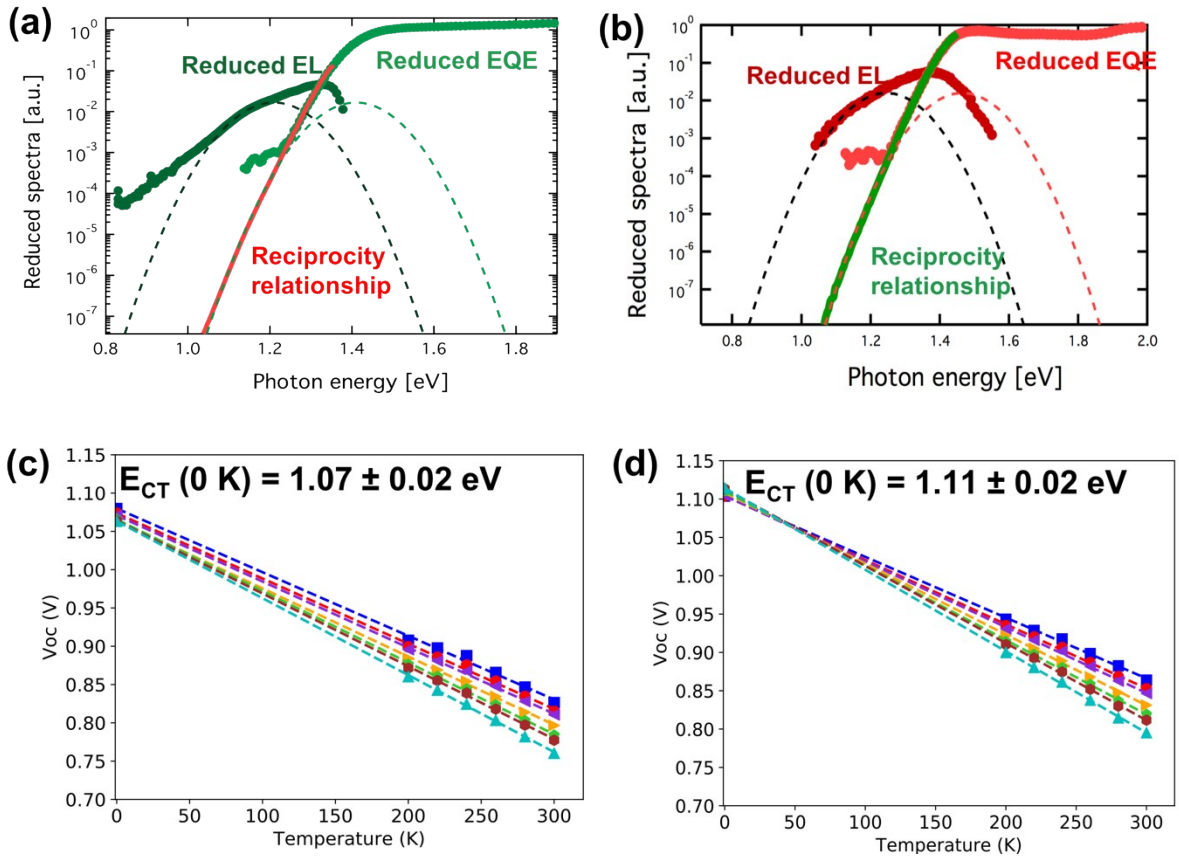

Fig. S4 (a) Simultaneous fitting of the reduced EQE_{PV} and EL spectra in the 1% LMWF PM6:Y6 blend; reciprocity relationship between EQE_{PV} and EL from **Equation S3** was used to calculate the EQE_{PV} down to 10^{-7} shown by the red solid line, the fitting parameters used were: $\lambda = 0.10$ eV, $E_{CT} = 1.31$ eV, $f = 3.0 \times 10^{-3}$ eV^2. **(b)** Simultaneous fitting of the reduced EQE_{PV} and EL spectra in the 52% LMWF PM6:Y6 blend; reciprocity relationship between EQE_{PV} and EL from **Equation S3** was used to calculate the EQE_{PV} down to 10^{-7} shown by the red solid line, the fitting parameters used were: $\lambda = 0.11$ eV, $E_{CT} = 1.35$ eV, $f = 3.0 \times 10^{-3}$ eV^2. Temperature-dependent V_{OC} for (c) 1% LMWF PM6:Y6 blend and (d) 52% LMWF blend measured at seven different light intensities (0, 0.2, 0.3, 0.5, 0.7, 0.8, and 1 OD) and extrapolated to 0 K for an estimate of the E_{CT} at 0 K.

Radiative and non-radiative recombination analysis:

Losses due to recombination (E_{CT} to V_{OC}), which can be divided into radiative (ΔV_{rad}) and non-radiative losses ($\Delta V_{non\text{-}rad}$), are quantified using **Equation S4**. The loss due to radiative recombination can be calculated based on the Marcus fitting parameters f, λ, and E_{CT} as shown in **Equation S5**. Using the fit parameters obtained from **Equations S2** and **S3**, we calculate the losses due to radiative recombination in the 1% LMWF PM6:Y6 blend system from **Equation S5** to be 0.199 ± 3 eV. From EQE_{EL} measurements and by plugging into this value in **Equation S6**, losses due to non-radiative recombination are measured to be 0.286 ± 3 eV; these results have been reported in previous literature.[7] For the 52% LMWF blend, the radiative recombination losses were calculated to be 0.220± 2 eV, and the non-radiative recombination losses are measured to be 0.285 ± 3 eV. The complete voltage losses due to charge transfer and recombination are summarized in the voltage loss diagrams below (**Fig. S5**).

$$V_{OC} = \frac{E_{CT}}{q} - \Delta V_{rad}(T) - \Delta V_{nonrad}(T) \tag{S4}$$

$$\Delta V_{rad}(T) = -\frac{kT}{q} ln\left(\frac{J_{SC} h^3 c^2}{f q 2\pi \left(E_{CT} - \lambda\right)}\right) \tag{S5}$$

$$\Delta V_{nonrad}(T) = -\frac{kT}{q} ln(EQE_{EL}) \tag{S6}$$

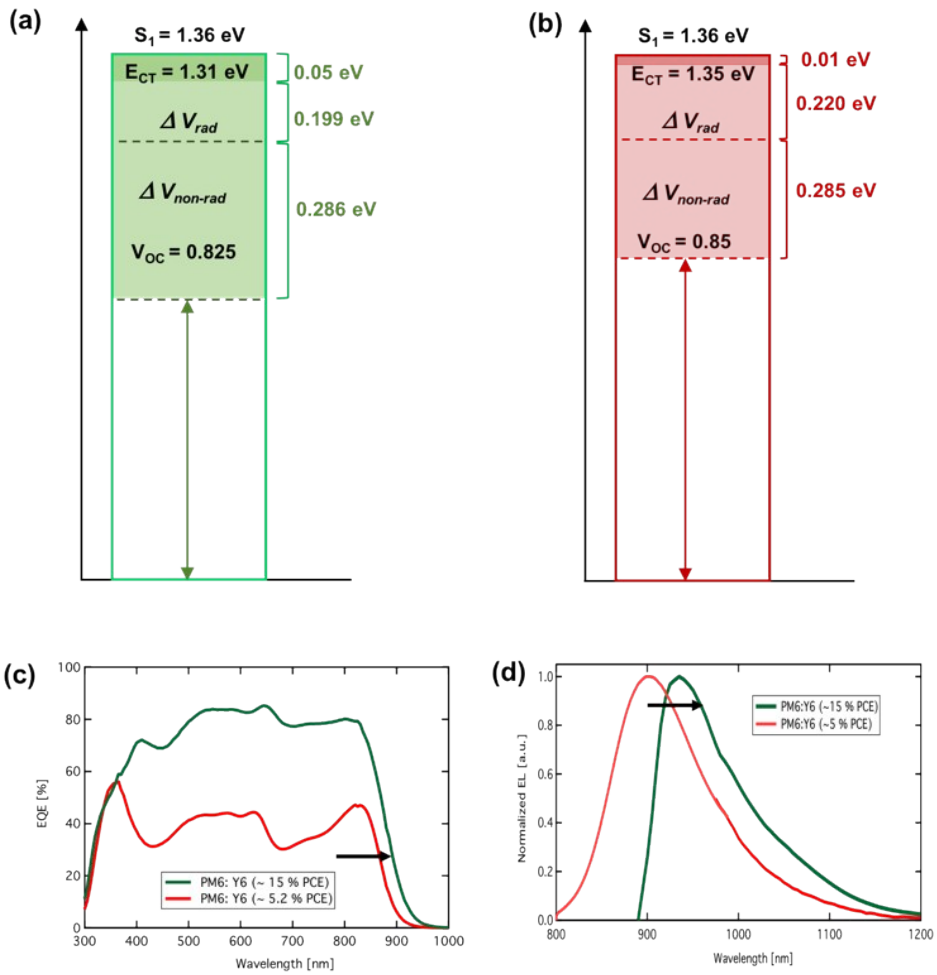

Fig. S5 Voltage loss contributions obtained via methods described in a previous report[7] for (a) 1% LMWF and (b) 52% LMWF blends. (c) EQE and (d) EL spectra of the two blend systems.

3. GIWAXS analyses of neat compounds and BHJ blend films

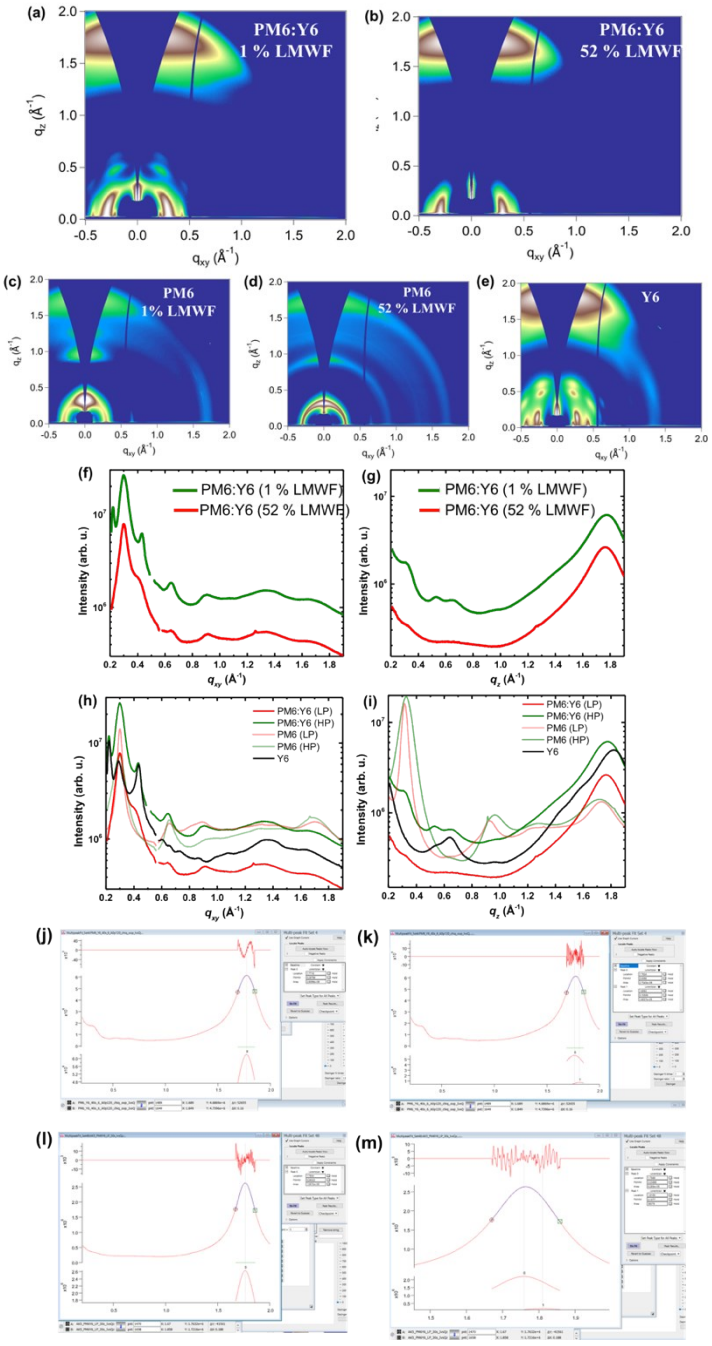

Fig. S6 2D GIWAXS spectra of (a) 1% LMWF PM6:Y6 blend, (c) 52% LMWF PM6:Y6 blend, (c) neat PM6 1% LMWF (d) neat PM6 52% LMWF, and (e) Y6. (f-i) Corresponding in-plane and out-of-plane line cuts of neat and blend films. Peak fittings for the 1% LMWF PM6:Y6 blend: (j) 1-peak fitting and (k) 2-peak fitting. Peak fittings for the 52% LMWF PM6:Y6 blend: (l) 1-peak fitting and (m) 2-peak fitting.

Table S2. GIWAXS parameters including in-plane and out-of-plane d-spacing, π-π and lamellae stacking distances obtained from the analyses GIWAXS patterns.

PM6:Y6 1% LMWF blend

Q_{xy} (Å^{-1})	d (nm)	L_c (nm)	Q_z (Å^{-1})	d (nm)	L_c (nm)
0.22	2.85	26	1.75	0.36	2.0
0.29	2.14	11	1.81	0.35	4.0
0.31	2.03	8.0	$Q_{off\text{-}axis}$ (Å^{-1})	d (nm)	L_c (nm)
0.43	1.46	6.0	0.518	1.21	5.0

PM6:Y6 52% LMWF blend

Q_{xy} (Å^{-1})	d (nm)	L_c (nm)	Q_z (Å^{-1})	d (nm)	L_c (nm)
0.29	2.16	18	1.76	0.36	2.0
0.30	2.07	12			
0.38	1.66	2.0			

PM6 1% LMWF

Q_{xy} (Å^{-1})	d (nm)	L_c (nm)	Q_z (Å^{-1})	d (nm)	L_c (nm)
0.30	2.12	5.0	0.33	1.92	5.0
0.66	0.96	5.0	0.97	0.65	3.0
1.69	0.37	2.0	1.29	0.49	1.0
			1.71	0.37	1.5

PM6 52% LMWF:

Q_{xy} (Å^{-1})	d (nm)	L_c (nm)	Q_z (Å^{-1})	d (nm)	L_c (nm)
0.30	2.09	12	0.32	1.99	10
0.66	0.96	4.0	0.93	0.68	4.0
0.86	0.71	4.0	1.73	0.36	2.0
1.70	0.37	2.0			

Y6:

Q_{xy} (Å^{-1})	d (nm)	L_c (nm)	Q_z (Å^{-1})	d (nm)	L_c (nm)
0.22	2.82	25	1.82	0.35	2.0
0.29	2.17	10			
0.43	1.45	14			
1.36	0.46	1.0			

GIWAXS measurements were performed on both the PM6:Y6 blend film and its neat components to provide insight into the molecular ordering within these films. The 2-D GIWAXS 1D linecuts corresponding to the in-plane (q_{xy}) and out-of-plane (q_z) scattered intensities are shown. The coherence lengths (L_c) represent the distance over which each scattering feature is maintained within their respective directions. These values are calculated through the Scherrer equation. Due to not having a proper calculation of the specific uncertainty, we have rounded off the reported L_c values to the nearest nm.

Neat films: The neat film of Y6 orients face-on with π-π stacking at 1.82 q_z (d: 0.35 nm, L_c: 2.24 nm), and lamellar stacking at 0.22 q_{xy} (d: 2.82 nm, L_c: 24.47 nm) which produces higher order reflections at 0.43 and 1.36 q_{xy}. The face-on orientation implies the long π-conjugated backbones are lying flat along the substrate with stacks of similarly oriented molecules extending in the direction normal to the substrate. This orientation favors transport in the direction normal to the substrate. Ordered features aligned neither in-plane nor out-of-plane produce off-axis scattering centered at 0.31 q (61.1 °X) and 0.53 q (27.3 and 22.3 °X). Because this feature is close to the substrate surface, it appears in the in-plane line cut near 0.29 q_{xy}.

Both the 1% and 52% PM6 neat films display weak scattering from π-π stacking near 1.7 q_z and intense bimodal scattering at the low q value of 0.3 $Å^{-1}$ (d: 2.1 nm) with higher order diffraction peaks near 0.66 q_{xy} and 0.93 q_z. This suggests that the donor material does not orient strictly face-on. The weak scattering observed near 1.7 q_{xy} further supports the more isotropic nature of this material as this is due to π-π stacks which are lying in the plane of the substrate. The most notable difference between the two batches of donor material is that the long-distance (real-space) isotropic stacking in the low performance PM6 extends for a distance roughly twice as long as that in the high performance PM6 as indicated by the L_c values. Long-distance real-space stacking typically corresponds to lamellar end-to-end stacks which do not transport charges as efficiently as the closely spaced π-π stacks. Isotropic orientation in this feature may hinder anisotropic charge transport between electrodes. The longer these features are, the more dominant isotropic charge transport may become, possibly contributing to some of the decrease in performance for the low molecular weight PM6.

Blend films: It is notable that in the 52% LMWF PM6:Y6 blend, π-π stacking is only observed for the PM6 donor at 1.76 q_z (d: 0.36 nm, L_c: 2.32 nm). In a previous study, this blend peak was near 1.75 q_z and assigned to Y6 in light of literature reports for Y6 π-π stacking at a similar value.[7,24] The presence of two π-π stacking peaks in the high performance blend and the additional measurements of the neat materials provide reasons to assign the PM6 π-π stacking to those peaks near 1.75 q_z in both blends. The π-π stacking from Y6 should be re-assigned as that present at 1.81 q_z (d: 0.35, L_c: 3.89 nm) in the 1% LMWF PM6:Y6 blend. The inability to resolve a scattering peak in the 52% LMWF blend corresponding to Y6 π-π stacking suggests that this feature is either not present or is present in a relatively small volume so that its resulting scattering is at an insufficient intensity to be identified separately.

The in-plane stacking peaks observed in the 52% LMWF PM6:Y6 blend are at 0.3 q_{xy} (d: 2.09 nm, L_c: 8.80 nm) which may result from features in both blends, and 0.38 q_{xy} (d: 1.66 nm, L_c: 2.12 nm) resulting from Y6. PM6 is able to contribute to the 0.3 q_{xy} peak due to its lamellar scattering; however, scattering at this distance from Y6 is due to off-axis scattering. Both of these stacking features are maintained for slightly longer distances within the 52% LMWF PM6:Y6 blend as evidenced by the L_c values. However, the 1% LMWF PM6:Y6 blend contains additional lamellar scattering from the acceptor at 0.22 q_{xy} (d: 2.85 nm, L_c: 26.30 nm) and 0.43 q_{xy} (d: 1.46 nm, L_c: 5.91 nm) in addition to the off-axis acceptor scattering near 30° X from the substrate normal. This information provides evidence that the acceptor ordering is better maintained in the 1% LMWF PM6:Y6 blend.

4. Parameters obtained from RSoXS analysis

Table S3. RSoXS parameters obtained from fitting the RSoXS profiles.

Sample	Peak position (nm^{-1})	Long period (nm)	Root-mean-square (RMS) composition variation
1 % LMWF	0.112	56	0.84
52 % LMWF	0.050	126	1

5. Solid state 1D and 2D NMR spectra of neat compounds and blends

A comparison of 1D ^{1}H MAS NMR spectra of the neat Y6 acceptor, the two different batches of PM6 (1% and 52% LMWF) donor polymers, and their respective BHJ blends is given in Fig. S7. In all cases, ^{1}H signals corresponding to aliphatic and aromatic moieties are clearly resolved in the ^{1}H MAS spectra of neat PM6 and Y6 compounds, however, the ^{1}H MAS spectra of BHJ blends exhibited severely overlapped signals that hindered accurate assignments of the distinct aromatic and aliphatic ^{1}H sites associated with PM6 and Y6 molecules.

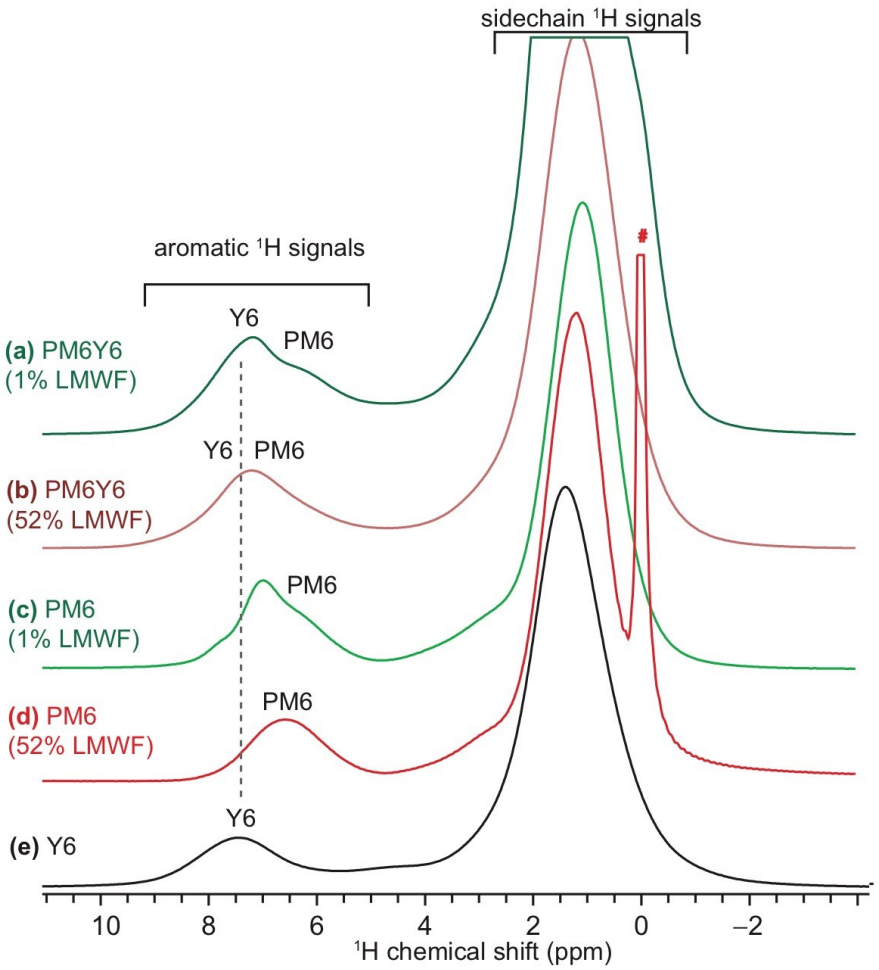

Fig. S7 Comparison of solid-state 1D ^{1}H NMR spectra of different batches of PM6 donor polymers, Y6 acceptor and their blends acquired at 21.1 T (60 kHz MAS). (a) PM6:Y6 blend with 1% LMWF, (b) PM6:Y6 blend with 52% LMWF, (c) PM6 with 1% LMWF, (d) PM6 52% LMWF, and (e) Y6 acceptor. # denotes residual solvent signal

Fig. S8 compares the 1D ^{19}F MAS NMR spectra obtained for PM6:Y6 blends consisting of 1% and 52% LMWF PM6 donor polymers. Intrinsically high sensitivity and spectral resolution associated with ^{19}F MAS NMR enable different distributions of ^{19}F sites associated with Y6 and

PM6 moieties to be detected and identified in the PM6:Y6 blends.[7] In PM6:Y6 blends with different LMFWs, the ^{19}F signals at −131 ppm were attributed to the ^{19}F sites in fluorinated thiophene groups of the PM6 donor polymer. The broad distributions of ^{19}F signals centered at −124 ppm were ascribed to the local environments of ^{19}F sites in the end groups of the Y6 acceptor molecules. It is noteworthy the ^{19}F MAS NMR spectrum of neat Y6 exhibited partially resolved signals at −120 ppm and −124 ppm, suggesting different distributions of ^{19}F chemical shifts,[7] which could be correlated to the different structural orders observed by GIWAXS measurements and analysis.[7,24] In the both high and low performing PM6:Y6 BHJ blends, the Y6 moieties showed a ^{19}F signal at −124 ppm, instead of two different ^{19}F signals as described above, indicating the improved Y6 molecular order in the BHJ blends compared to the neat Y6 molecules. By comparison, the ^{19}F chemical shift of fluorinated thiophene groups in the PM6 polymer at −131 ppm reveals identical local bonding environments in both PM6:Y6 blends, which is consistent with the ^{19}F chemical shift (−131 ppm) of fluorinated thiophene groups in the neat PM6 polymer.[7] These results are further corroborated by 2D ^{19}F-^{19}F spin-diffusion (SD) measurements and analyses (Fig. S8c,d).

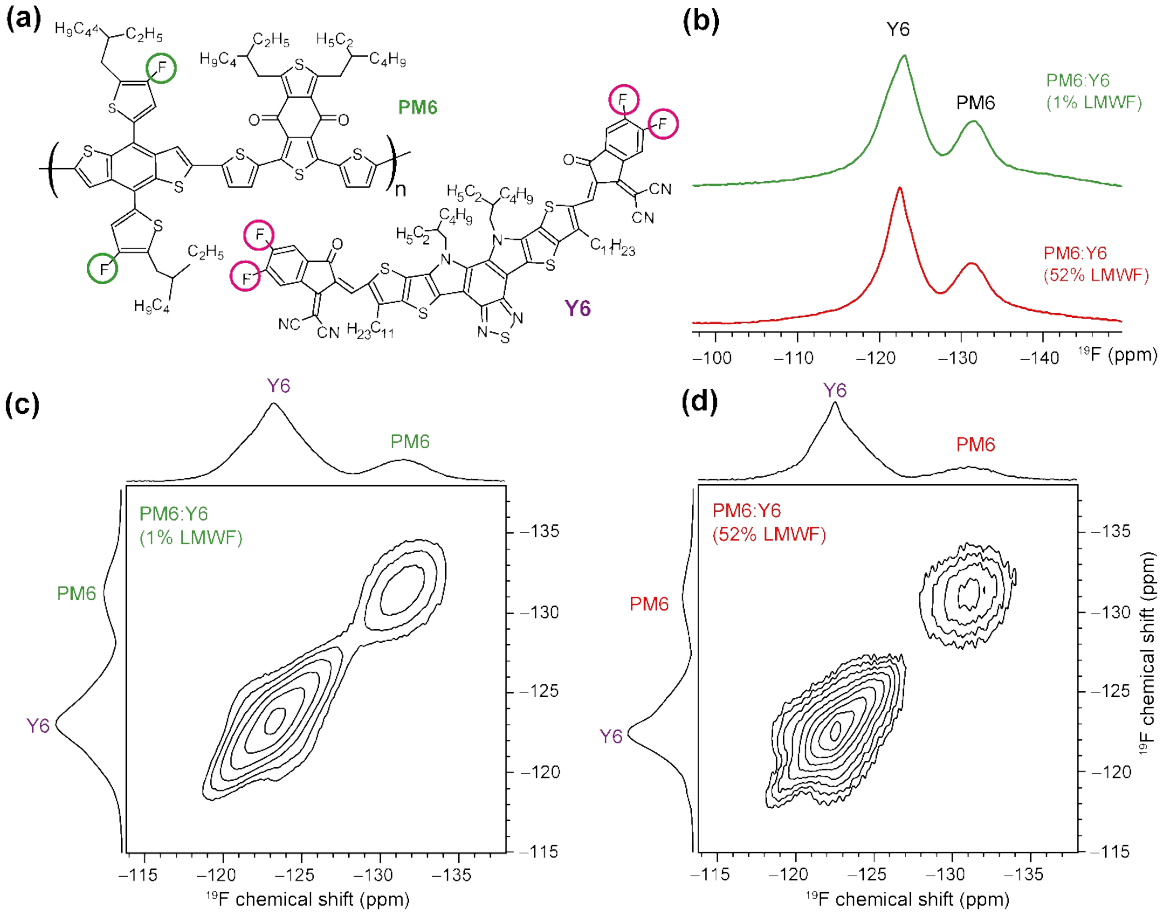

Fig. S8 Comparison of solid-state 1D ^{19}F NMR spectra, and 2D ^{19}F-^{19}F correlation spectra of different batches of PM6:Y6 blends acquired at 21.1 T (60 kHz MAS); (a) schematic structures of PM6 and Y6, (b) 1D ^{19}F MAS NMR spectra of PM6:Y6 blend with 52% and 1% LMWFs, (c) 2D ^{19}F-^{19}F correlation of PM6:Y6 blend with 1% LMWF of PM6, and (d) 2D ^{19}F-^{19}F correlation of PM6:Y6 blend with 52% LMWF of PM6.

In a 2D ^{19}F-^{19}F spin-diffusion experiment, the ^{19}F magnetization exchange between spatially proximate ^{19}F sites is probed as a function of mixing time, also referred to as spin-diffusion time, which leads to on-diagonal self-correlation and off-diagonal cross-correlation intensities. The off-diagonal 2D correlation peaks imply the magnetization exchange between different ^{19}F chemical shifts. 2D ^{19}F-^{19}F spectra of both the 1% LMWF and 52% LMWF blends exhibited self-correlation intensities along the diagonal corresponding to fluorine sites in PM6 (–131 ppm) and Y6 (–124 ppm) moieties, whereas no cross-correlation intensities between them were observed even when a long mixing time of 1 s was used. This confirms there is no magnetization exchange between the ^{19}F sites in PM6 and Y6 molecules in both high and low performing blends, suggesting that the effective spatial distance between fluorine atoms in the PM6 and Y6 molecules is greater than a nm, which would have shown a cross peak when they are closer to each other within 1 nm distance. This result rules out the possibility of intercalation of Y6 molecules in between PM6 polymer chains, which is corroborated by the GIWAXS patterns that showed π–π stacking interactions between Y6 molecules themselves and between PM6 polymers themselves in BHJ blends (Fig. S5). While the information obtained from the ^{19}F spectra is not sufficient enough to reveal differences in the more detailed D:A inter- and intramolecular interactions of the two blends, complementary insights into D:A contacts can be attained by analyzing 1D $^{13}C\{^{1}H\}$ cross-polarization (CP) MAS and 2D ^{13}C-^{1}H correlation NMR spectra of neat compounds and blends, as will be discussed in the subsequent sections.

A comparison of 1D $^{13}C\{^{1}H\}$ CP-MAS NMR spectra of neat Y6, PM6 (1% and 52% LMWF) and their blends is given in Fig. S8, which allows the signals corresponding to different carbon sites in the PM6 and Y6 molecules to be distinguished and identified. In a CP experiment, ^{1}H and ^{13}C nuclei are simultaneously excited and $^{1}H \rightarrow {}^{13}C$ polarization transfer is achieved in order to enhance the signal intensities of these latter. For neat Y6 and different batches of PM6 polymers consisting of 1% and 52% LMWFs, ^{13}C signals in the aliphatic regions at 12, 13 and 15 ppm are assigned to terminal methyl groups, and partially resolved signals in the range of 23-35 ppm and 42 ppm are attributed to methylene groups in the branched sidechains. In the aromatic region of the $^{13}C\{^{1}H\}$ CP-MAS spectra of different PM6 polymer batches, signals associated with the protonated and quaternary carbon atoms in thiophene, benzodithiophene and benzodithiophenedione moieties (120-142 ppm), fluorinated carbon sites in thiophene moieties (153 ppm), and carbonyl groups of benzodithiophenedione (178 ppm) are distinguished and identified. In comparison, the aromatic ^{13}C signals in the $^{13}C\{^{1}H\}$ CP-MAS spectrum of Y6 molecules, 115-120 ppm, 127-134 ppm, and 146-147 ppm are attributed to different aromatic carbon atoms. The signals at 153-154 ppm are attributed to fluorinated carbon sites in

difluorophenyl end groups and the signal at 178 ppm is attributed to carbonyl groups of the Y6 molecule. Even though the $^{13}C\{^{1}H\}$ CP-MAS spectra of the two PM6:Y6 blends mostly consist of severely overlapped frequencies originating from PM6 and Y6, signals corresponding to a few specific ^{13}C sites, e.g. carbonyl groups, can still be identified and distinguished.

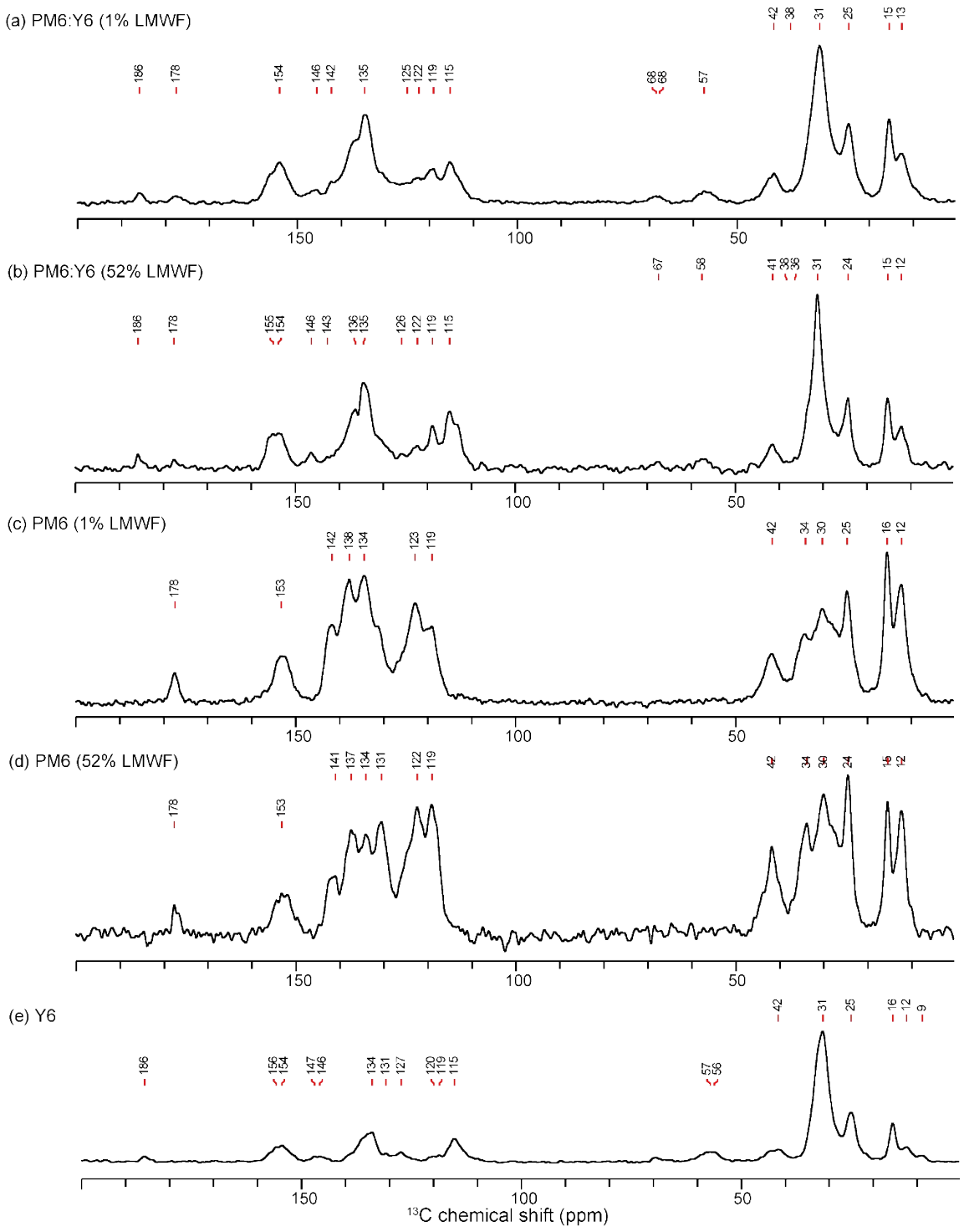

Fig. S9 Comparison of solid-state 1D $^{13}C\{^{1}H\}$ CP-MAS spectra of different batches of PM6 donor polymers and their blends acquired at 9.4 T (12.5 kHz MAS); (a) PM6:Y6 blend with 1% LMWF, (b) PM6:Y6 blend with 52% LMWF, (c) PM6 1% LMWF, (d) PM6 52% LMWF and (e) Y6 acceptor, acquired with 4 ms of CP contact time.

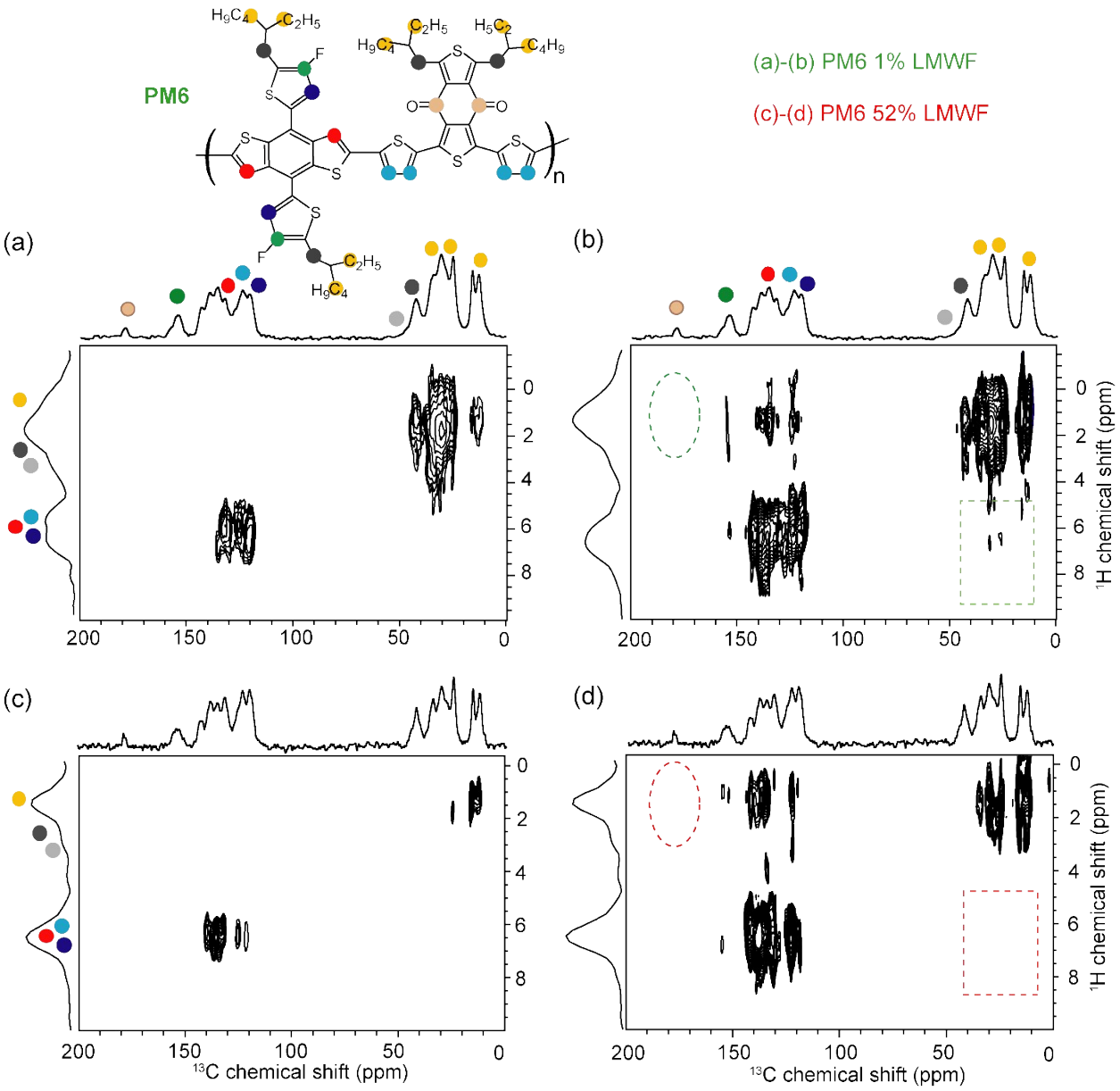

Fig. S10 Comparison of solid-state 2D ^{13}C-^{1}H HETCOR spectra of different batches of PM6 donor polymer acquired at 9.4 T (12.5 kHz MAS) with 1% LMWF using (a) 0.1 ms and (b) 4 ms, and with 52% LMWF using (c) 0.1 ms and (d) 4 ms of CP contact times.

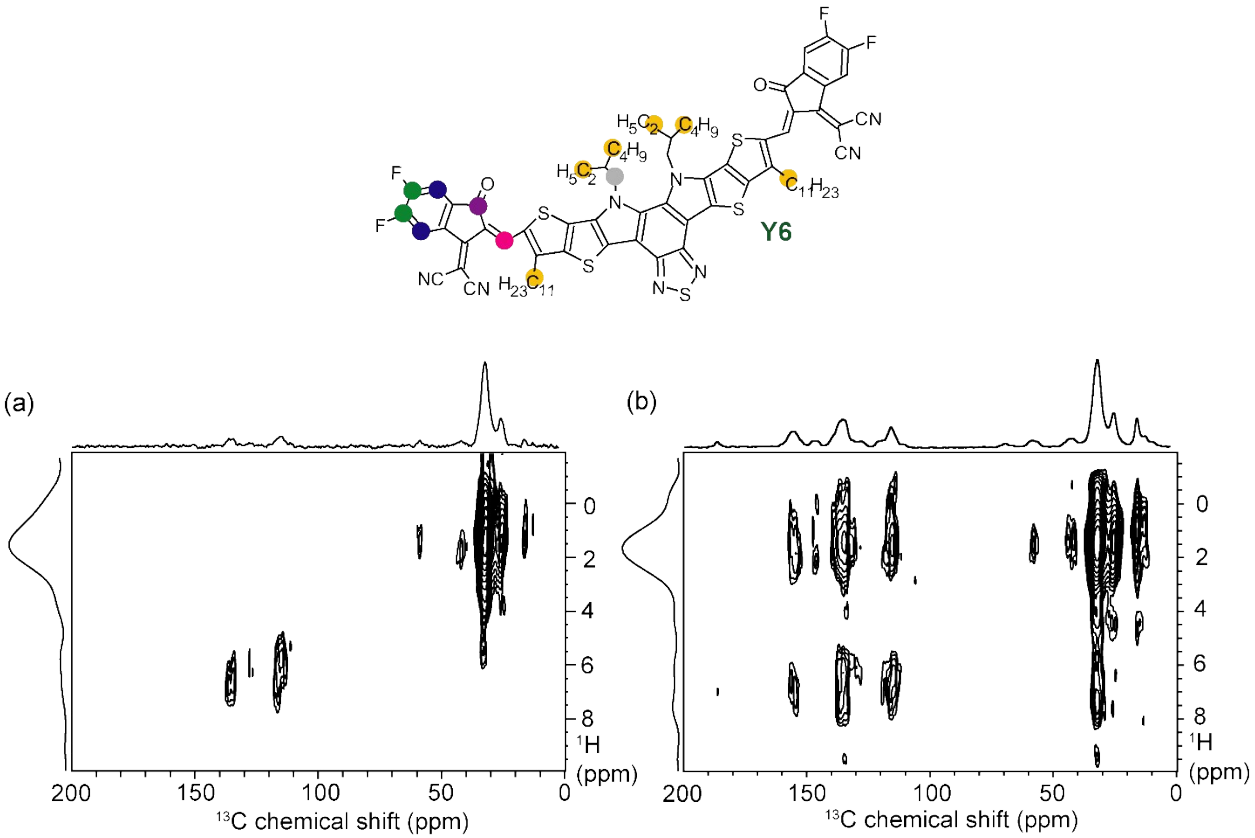

Fig. S11 Comparison of solid-state 2D ^{13}C-^{1}H HETCOR NMR spectra of neat Y6 material acquired at 9.4 T (12.5 kHz MAS) using (a) 0.1 ms and (b) 4 ms CP contact times.

6. Probing Charge Generation Dynamics

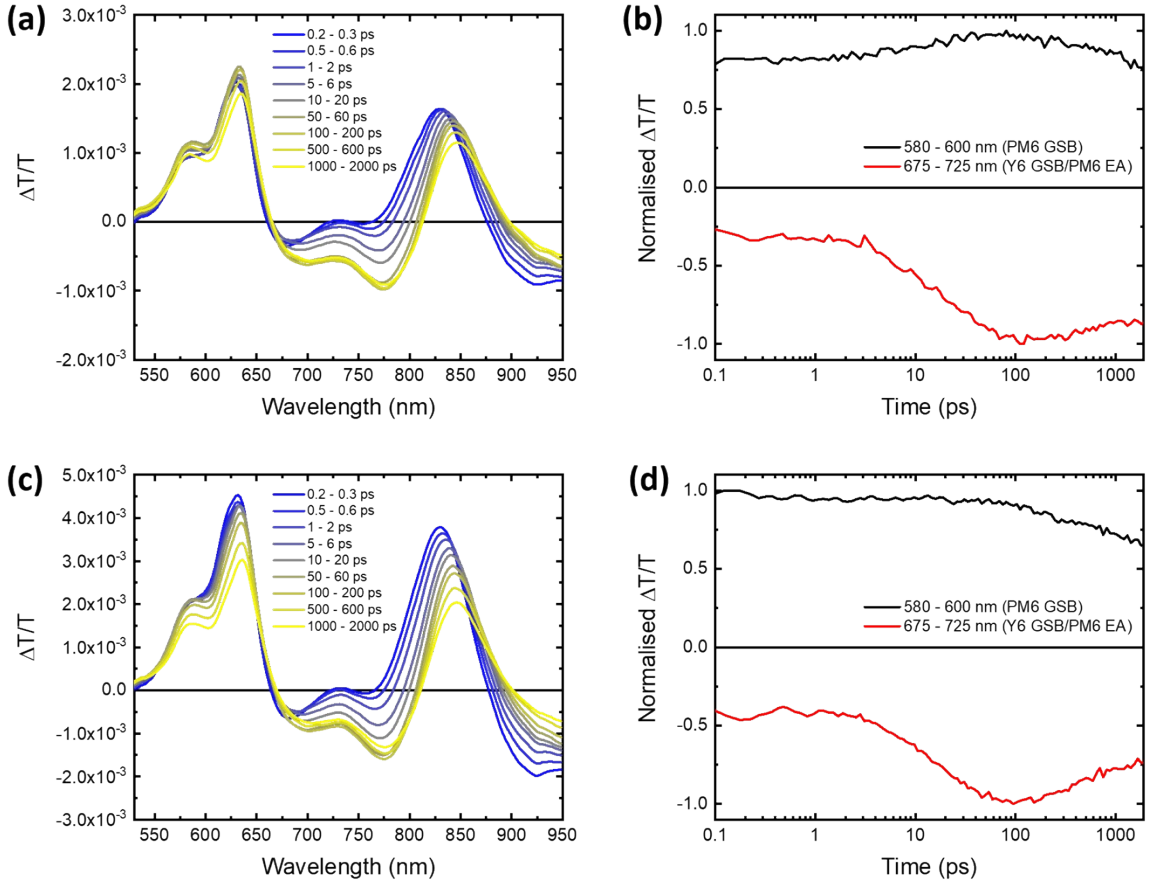

Fig. S12 Medium fluence (a) visible region TA spectra, (b) fitted kinetics of PM6:Y6 1% LMWF blend (pump: 580 nm and fluence: 2.76 μJ cm^{-2}). High fluence (c) visible region TA spectra, (d) fitted kinetics of PM6:Y6 1% LMWF blend (pump: 580 nm and fluence: 6.56 μJ cm^{-2}).

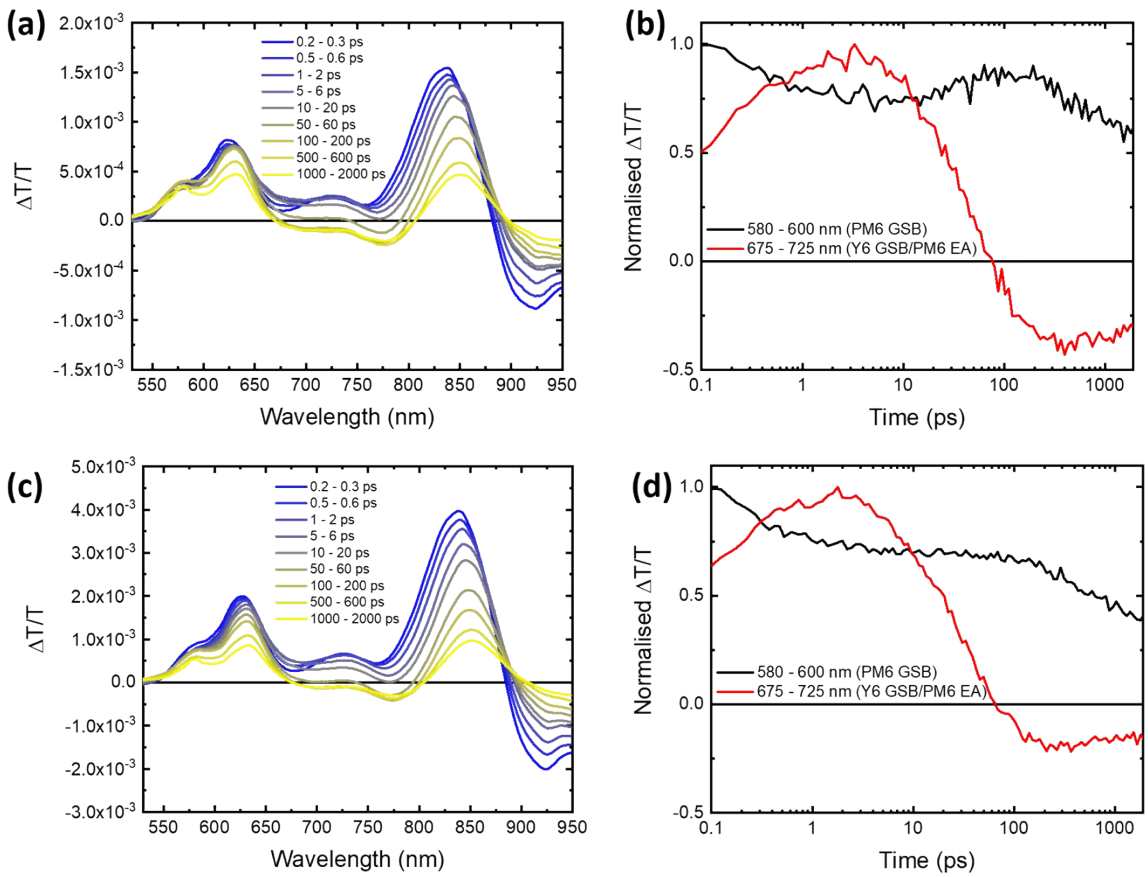

Fig. S13 Medium fluence (a) visible region TA spectra, (b) fitted kinetics of PM6:Y6 52% LMWF blend (pump: 580 nm and fluence: 2.53 μJ cm^{-2}). High fluence (c) visible region TA spectra, (d) fitted kinetics of PM6:Y6 52% LMWF blend (pump: 580 nm and fluence: 6.33 μJ cm^{-2}).

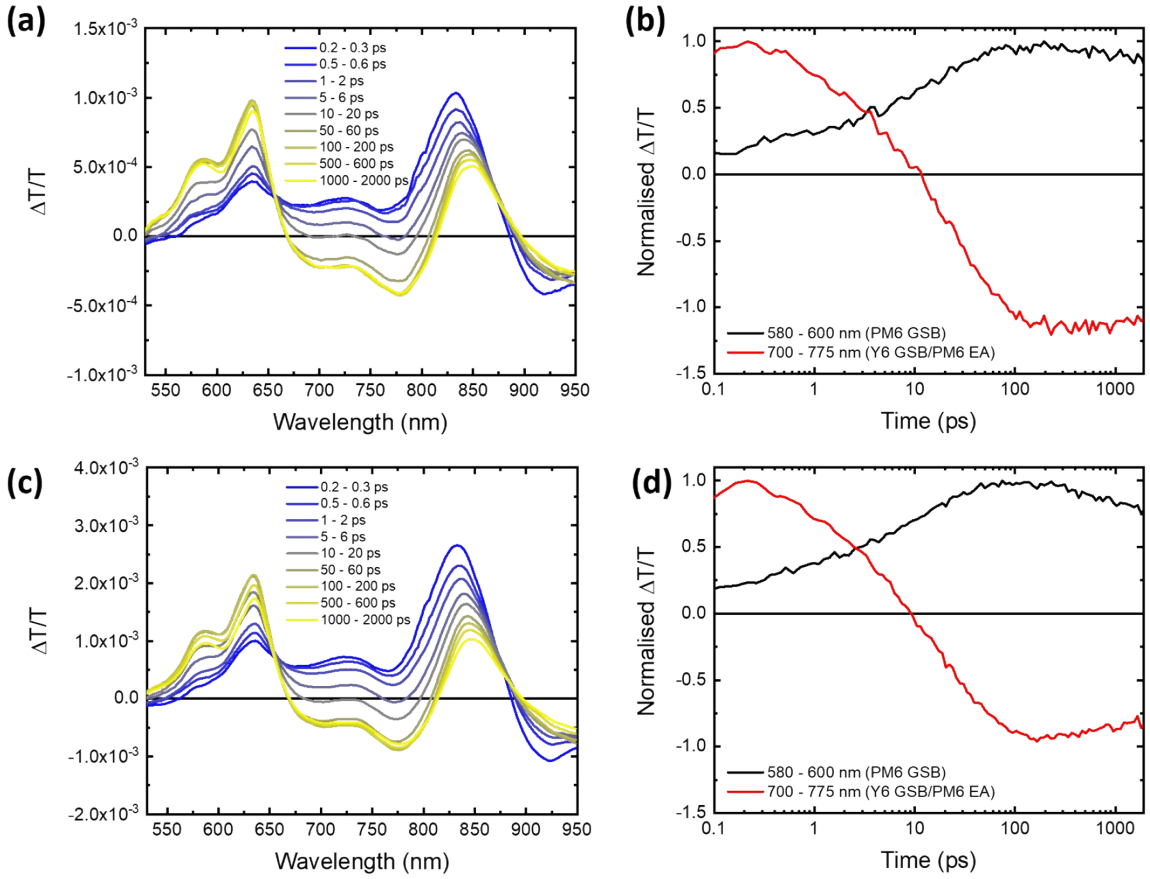

Fig. S14 Medium fluence (a) visible region TA spectra, (b) fitted kinetics of PM6:Y6 1% LMWF blend (pump: 800 nm and fluence: 1.00 μJ cm^{-2}). High fluence (c) visible region TA spectra, (d) fitted kinetics of PM6:Y6 1% LMWF blend (pump: 800 nm and fluence: 2.43 μJ cm^{-2}).

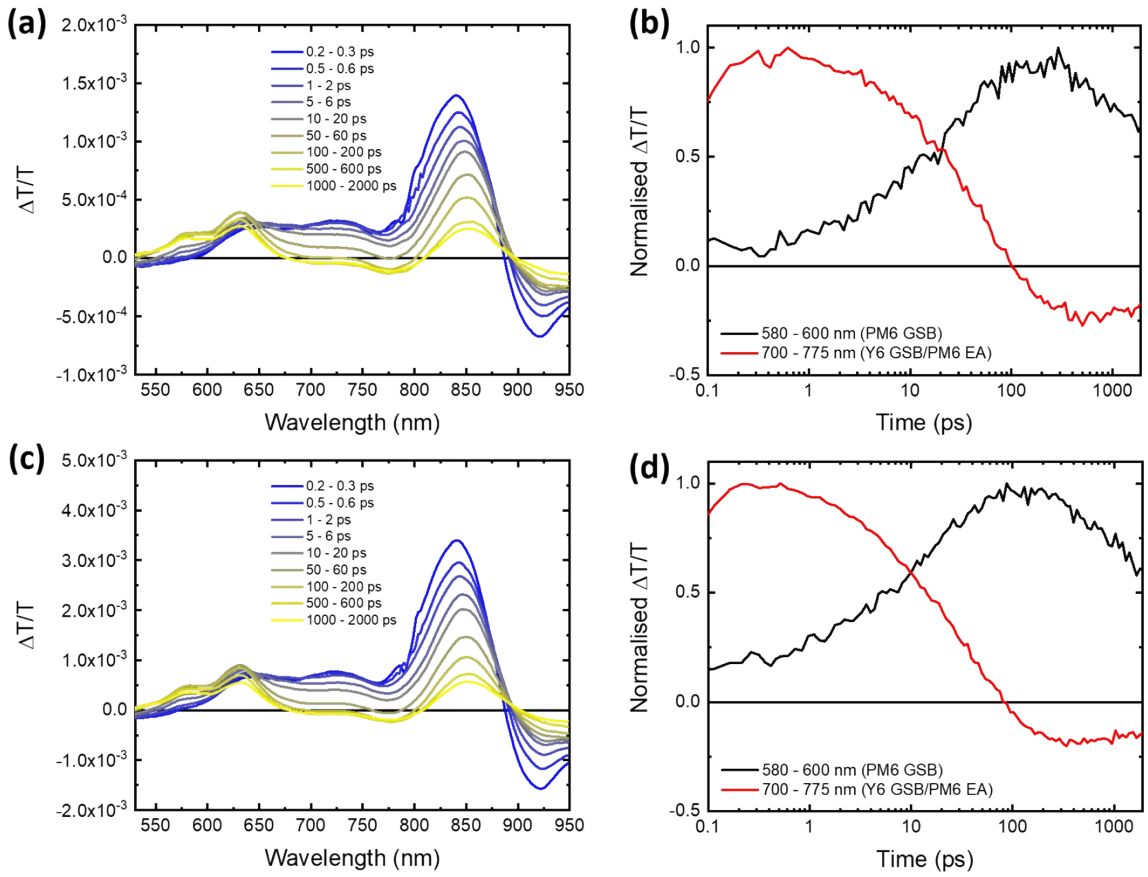

Fig. S15 Medium fluence (a) visible region TA spectra, (b) fitted kinetics of PM6:Y6 52% LMWF blend (pump: 800 nm and fluence: 1.27 μJ cm^{-2}). High fluence (c) visible region TA spectra, (d) fitted kinetics of PM6:Y6 52% LMWF blend (pump: 800 nm and fluence: 3.18 μJ cm^{-2}).

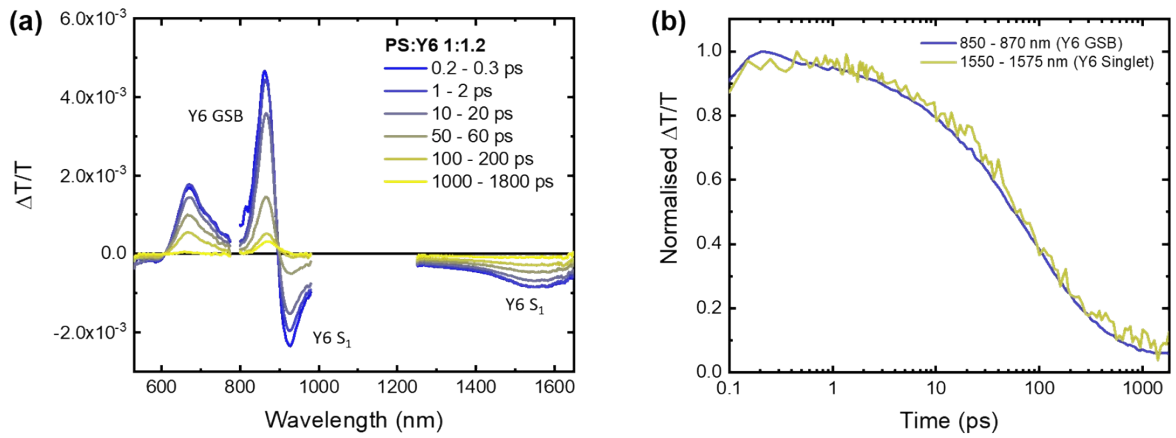

Fig. S16 (a) TA spectra and (b) fitted kinetics of Polystyrene:Y6 (pump: 800 nm and fluence: 1.8 μJ cm^{-2}).

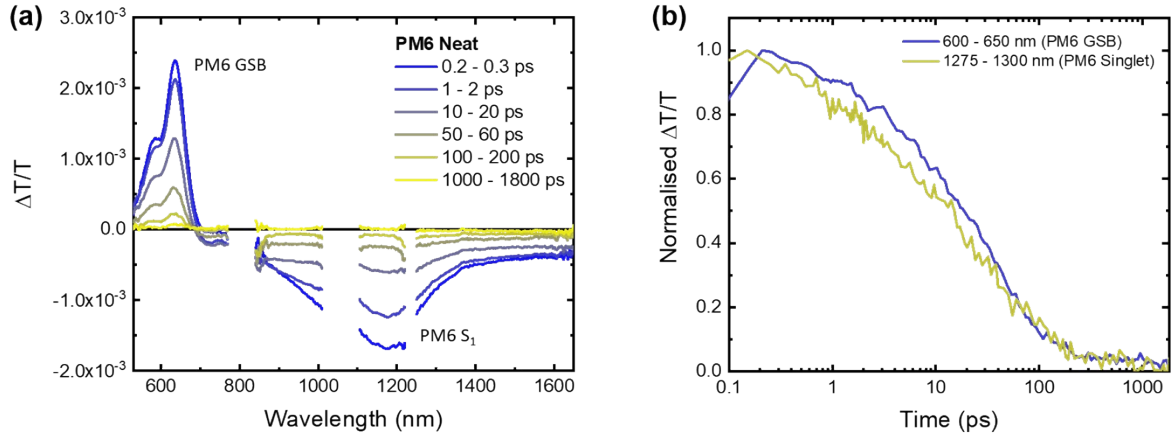

Fig. S17 (a) TA spectra and (b) fitted kinetics of 1% LMWF PM6 (pump: 532 nm and fluence: 3.1 μJ cm^{-2}).

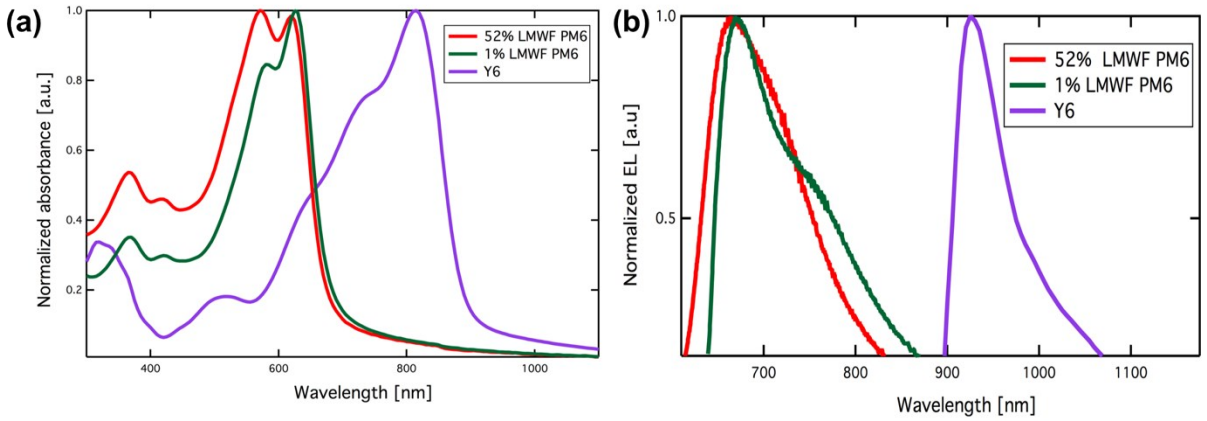

Fig. S18 (a) Normalized absorbance spectra of neat 52% LMWF PM6, 1% LMWF PM6, and Y6. (b) Normalised emission spectra of neat 52% LMWF PM6, 1% LMWF PM6, and Y6.

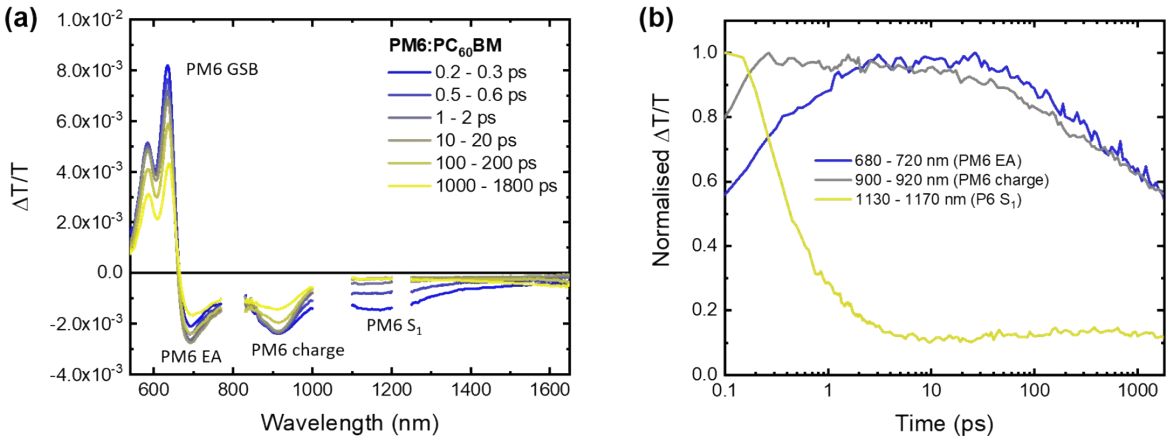

Fig. S19 (a) TA spectra and (b) fitted kinetics of PM6:PCBM (pump: 532 nm and fluence: 5.1 μJ cm^{-2}).

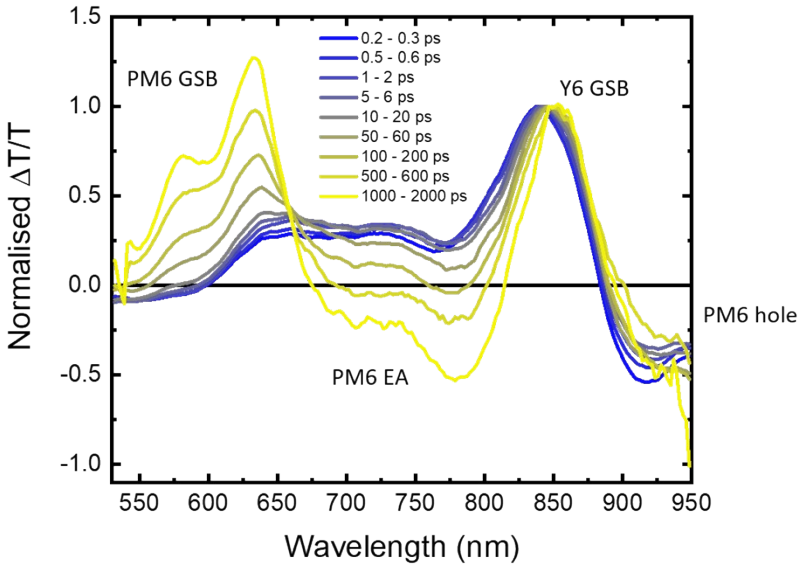

Fig. S20 (a) TA spectra of PM6:Y6 52% LMWF (pump: 800 nm and fluence: 0.5 μJ cm^{-2}).

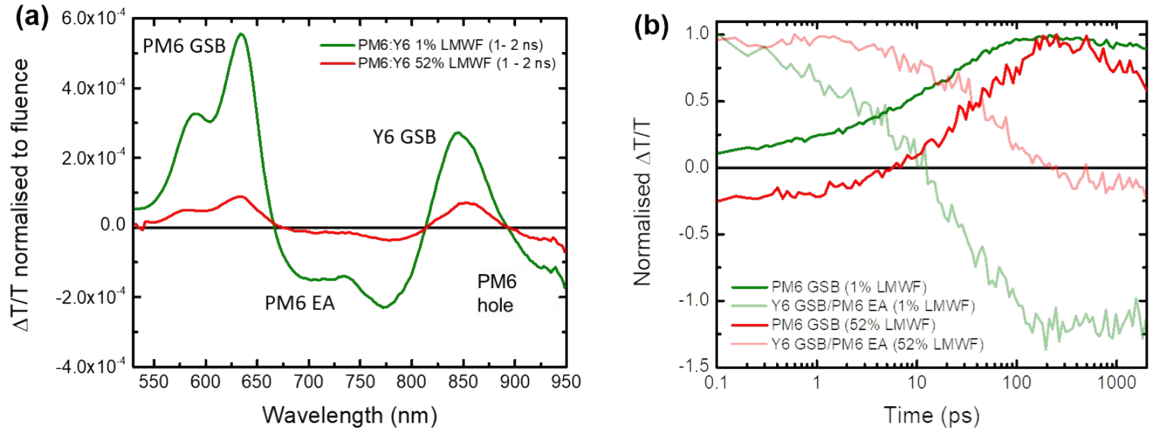

Fig. S21 Comparison of the PM6:Y6 1% and 52% LMWF blends (a) TA spectra at 1-2 ns normalized to fluence to account for the greater total number of excitons created in the 1% LMWF blend (due to the higher fluence) and (b) fitted kinetics.

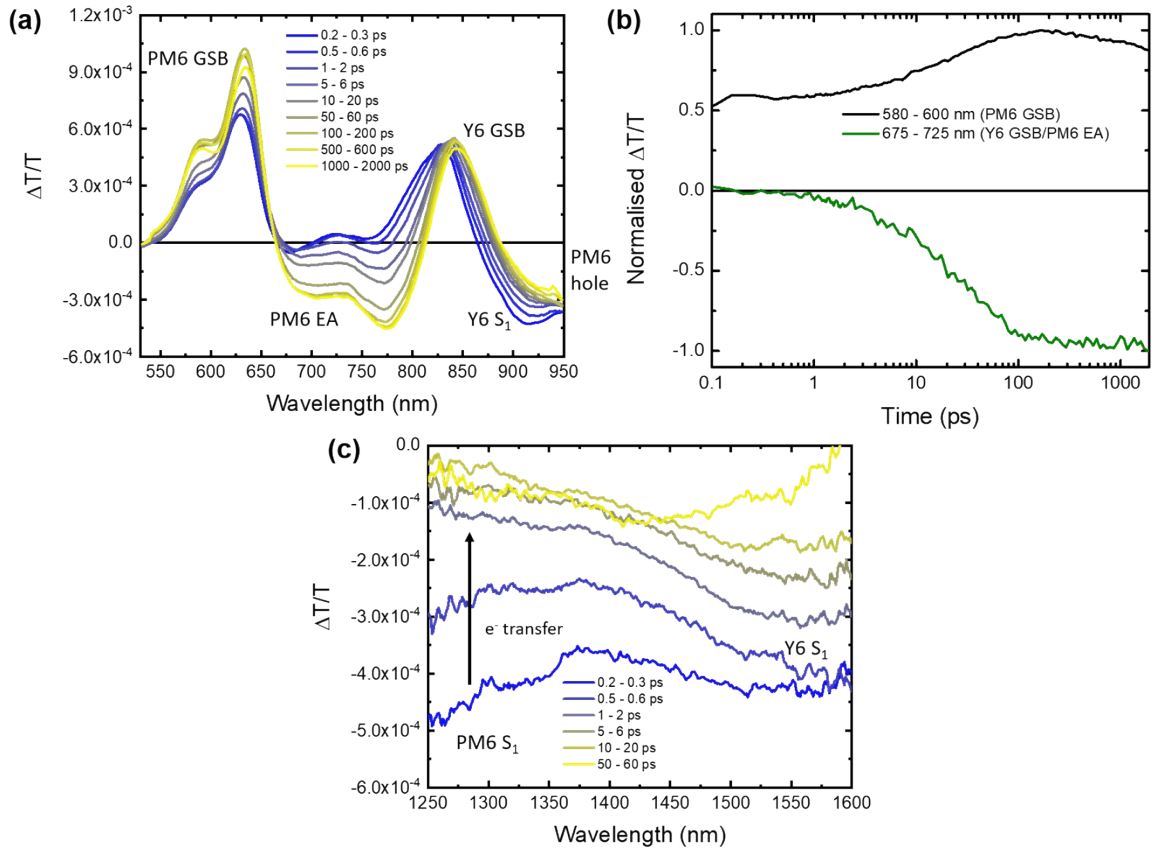

Fig. S22 (a) Visible region TA spectra, (b) fitted kinetics of PM6:Y6 1% LMWF blend (pump: 580 nm and fluence: 0.67 μJ cm^{-2}), and (c) Near IR TA spectra (fluence: 2.38 μJ cm^{-2}).

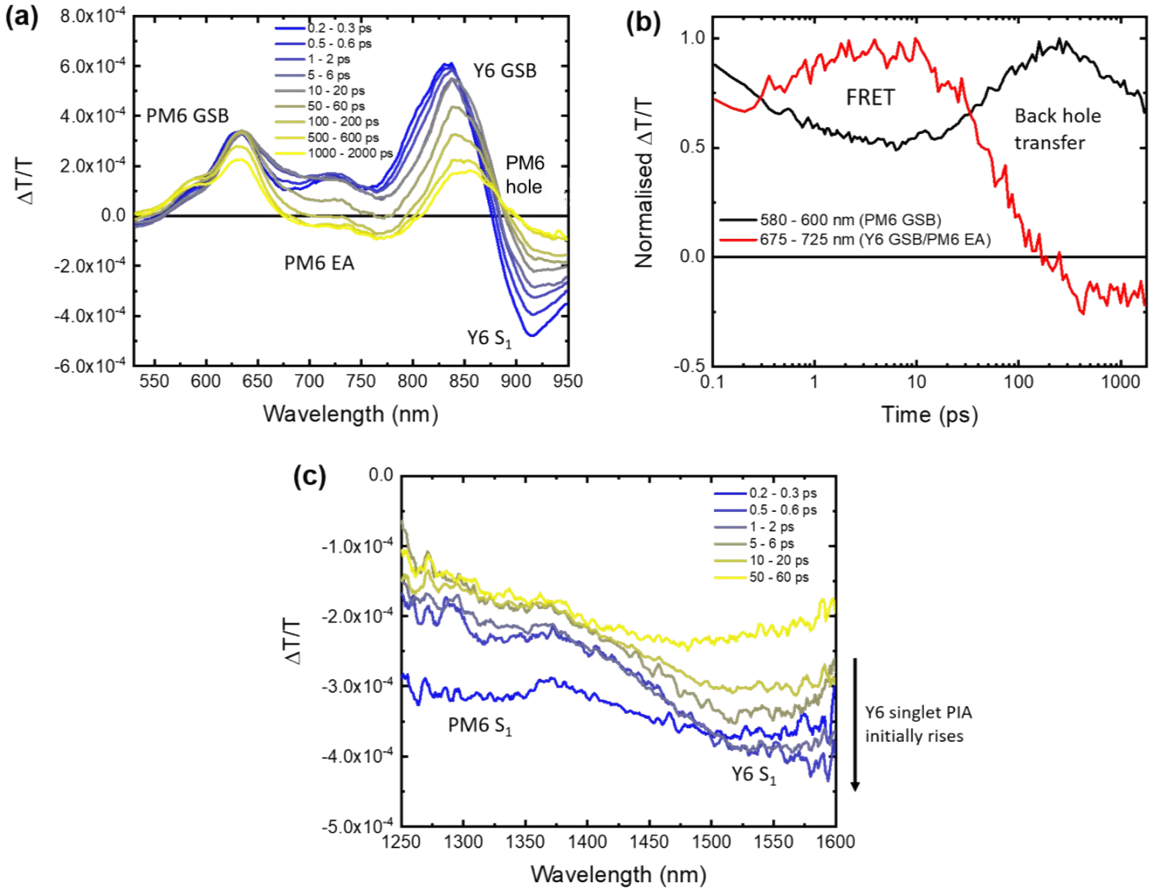

Fig. S23 (a) Visible region TA spectra, (b) fitted kinetics of PM6:Y6 52% LMWF blend (pump: 580 nm and fluence: 0.95 μJ cm^{-2}), and (c) Near IR TA spectra (fluence: 3.50 μJ cm^{-2}).

7. Non-geminate recombination and extraction dynamics

7.1. V_{OC} vs. ln (intensity) for a qualitative determination the dominant recombination mechanism

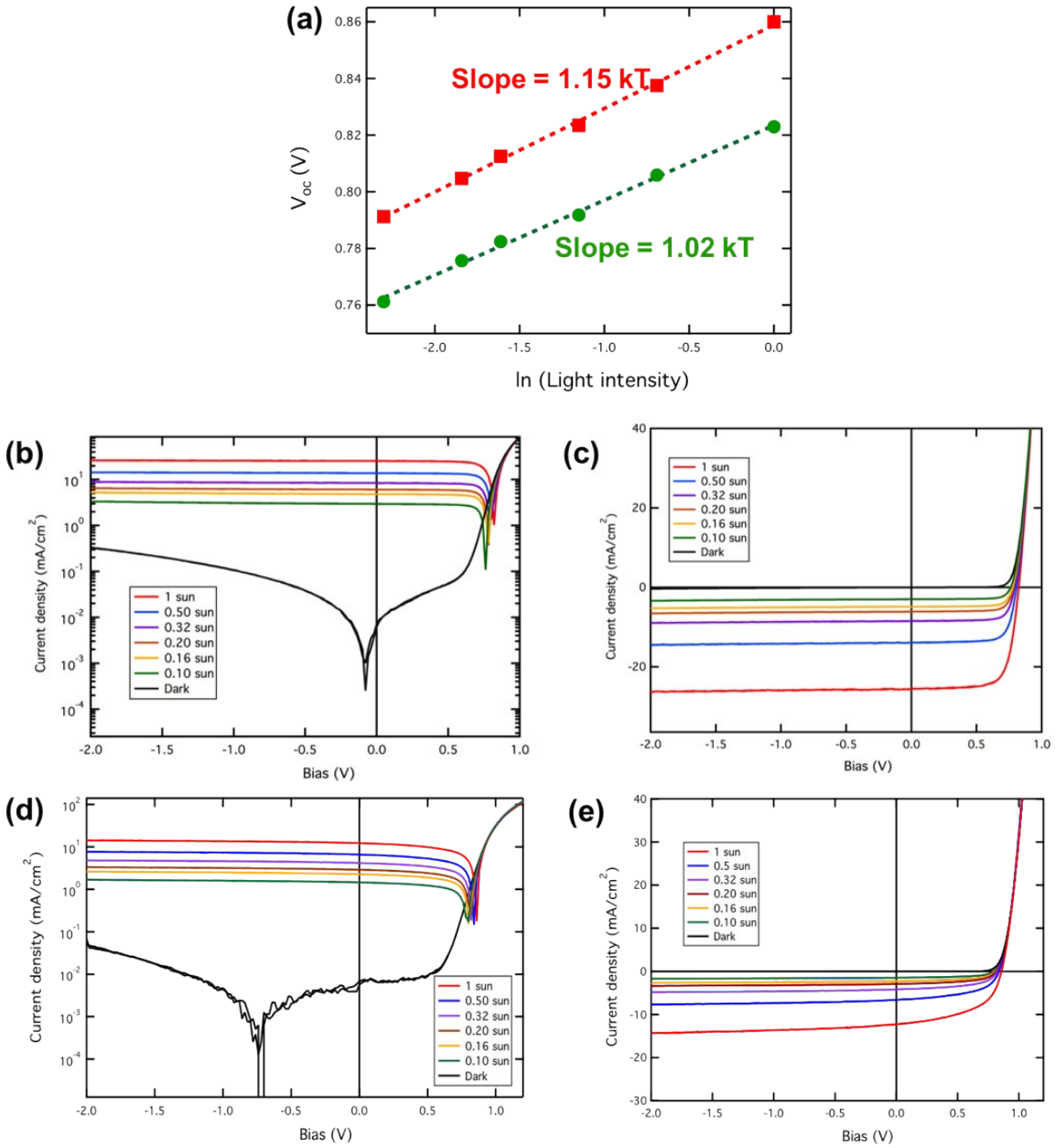

Fig. S24 (a) V_{OC} vs. ln(light intensity) plots for the 1% LMWF and 52% LMWF blend systems. *J-V* curves of the two blend systems plotted at varying light intensities on semi-log and linear scale for (a) 1% LMWF and (b) 52% LMWF PM6:Y6 blend systems.

7.2. Capacitance spectroscopy for determining charge carrier densities

The dielectric constants of the two blends were measured by capacitance spectroscopy at a reverse bias of -3 V and in the dark (Fig. S19). For this DC bias, there should be no frequency dependence of the capacitance. Then, the assumption is that the capacitance of the blend C_b measured under these conditions is equal to the geometric capacitance C_g, which would allow employing the following equation to calculate the dielectric constant ε_r:

$$\varepsilon_r = \frac{C_g L}{\varepsilon_0 A}, \tag{S7}$$

where L is the thickness of the active layer and A is the area of the device. To begin a quantitative analysis of the recombination dynamics, it is necessary to obtain values for the charge carrier density n. It is known that capacitance spectroscopy can be employed to determine the density of charge carriers in organic solar cells under illumination. Capacitance spectroscopy was performed to yield the charge carrier density n, *via* integration of the chemical capacitance using the following equations:

$$C_{chem} = C_b^{1sun} - C_b^{dark}, \tag{S8}$$

$$n(V_{cor}) = \frac{1}{qAL}\int_{V_{sat}}^{V_{cor}} C_{chem}\, dV_{cor}, \tag{S9}$$

where A is the area of the solar cell, L is the thickness, V_{sat} is the reverse bias at which the photocurrent saturates, and V_0 is the forward bias at which the photocurrent is equal to zero. In this analysis the capacitance in the bulk-heterojunction C_b at the plateau at frequencies of $\omega = 10$ kHz and $\omega = 50$ kHz for the low and high performing devices was chosen. It is assumed that the difference of C_b under illumination and in the dark is related to the density of photogenerated charge carriers (Fig. S19). Therefore, this difference equates to the chemical capacitance C_{chem}, as described in Equation S2.[25] This approach to determine the charge carrier density n does not require the addition of the saturated charge carrier density n_{sat}, in contrast to other approaches commonly used. The charge carrier density n then becomes available once the chemical capacitance is integrated over the voltage (Fig. S20a).

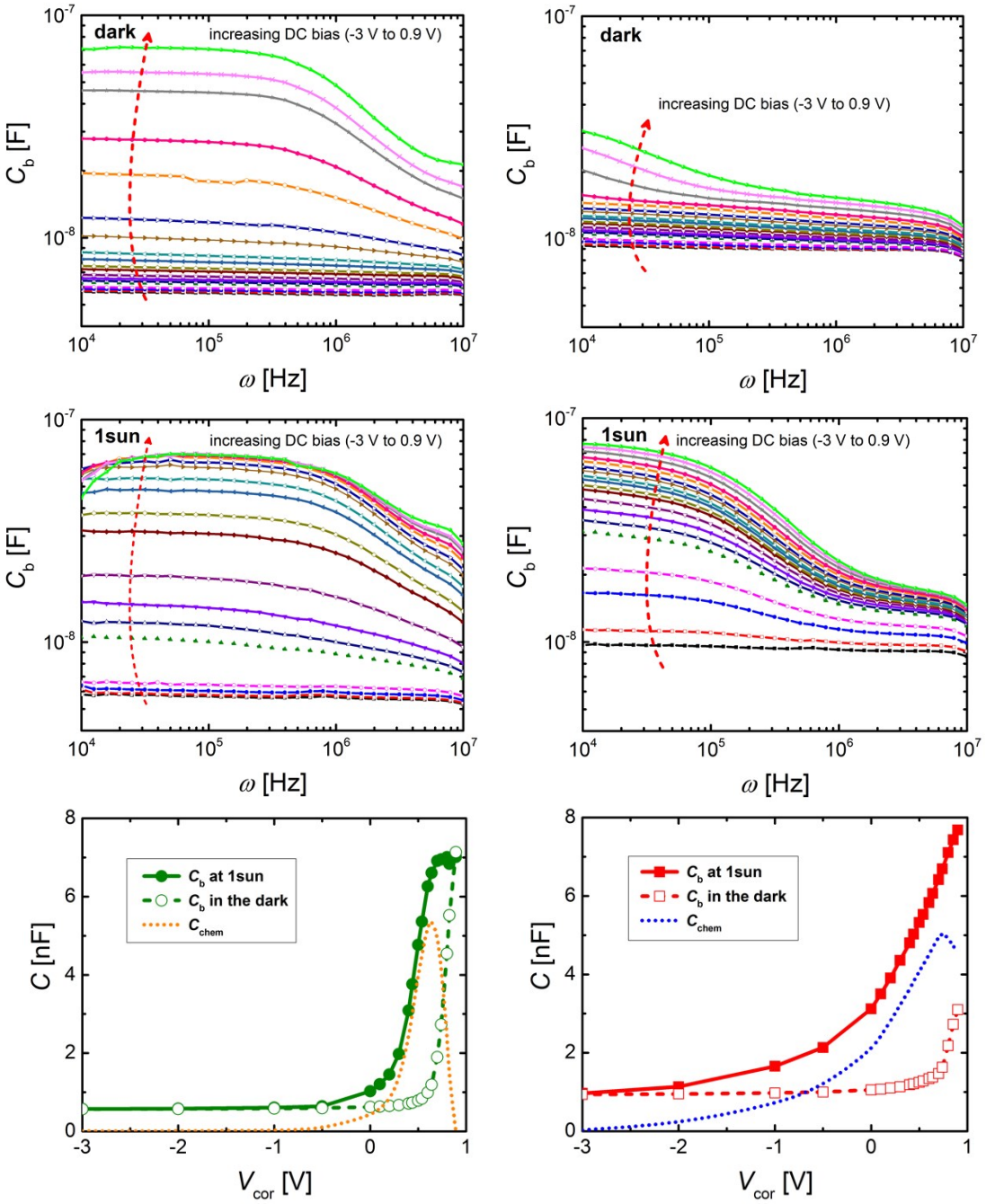

Fig. S25 Frequency dependent capacitance in the bulk-heterojunction C_b in the dark and under 1 sun illumination of the solar cells employing the high (LMWF = 1%; left column) and low (LMWF = 52%; right column) performing PM6 batches. The difference between the capacitance C_b at 1 sun illumination and in the dark at a specific frequency (LMWF = 1%: ω = 50 kHz; LMWF = 52%: ω = 10 kHz) is used to calculate the chemical capacitance C_{chem} (orange and blue dots) that is attributed to the photogenerated charge carriers within the bulk-heterojunction.

7.3. Determining effective mobilities under operating conditions

The calculation of a field and charge carrier dependent, effective mobility $\mu_{eff}(n,V)$ has been introduced by Albrecht *et. al.* as an alternative to the hole/electron mobility $\mu_{p/n}$ determined *via* the Mott-Gurney relationship of space-charge limited currents (SCLC) in single carrier devices.[26] It was argued that mobilities determined *via* SCLC measurements may be unreliable due to deviation from the expected thickness dependent behavior, the variation of electrode materials that may have an impact on the morphology, charge carrier densities and electric-fields that are larger in the SCLC regime in comparison to the normal operating conditions of a solar cell (ultimately leading to overestimated mobilities), and finally the fact that the motion of injected carriers is measured in contrast to photogenerated carriers. The use of such an effective mobility μ_{eff} is especially encouraged, if a strong dependence of the mobility on either the applied bias V, the charge carrier density n, or both can be expected. The effective mobility μ_{eff} can be calculated by employing the following equation:

$$\mu_{eff}(n,V_{cor}) = \frac{J(V_{cor}) \cdot L}{2qn(V_{cor}) \cdot [V_{cor} - V_0]}, \tag{S10}$$

where J is the current density, V_{cor} is the corrected voltage, V_0 is the voltage at which the photocurrent is equal to zero, L is the device thickness, q is the elementary charge, and n is the charge carrier density obtained from capacitance spectroscopy. The effective mobility μ_{eff} ideally relates to the two different types of mobility μ_n and μ_p *via* the following equation:

$$\mu_{eff} = \frac{2\mu_n\mu_p}{\mu_n + \mu_p}. \tag{S11}$$

The effective mobility of the low performing devices is more or less constant over the entire voltage range, as can be seen in **Fig. S20b**. In contrast, the high performing devices show a wider variability in the effective mobility values. In the subsequent analysis, the average mean of the determined effective mobility is used.

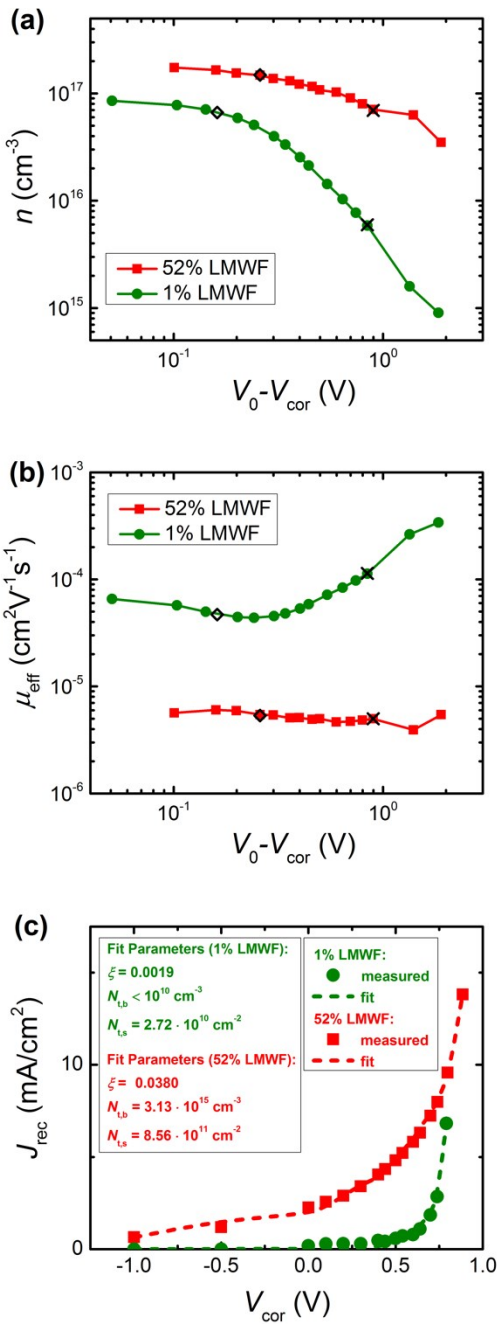

Fig. S26 (a) Charge carrier density n and (b) effective mobility μ_{eff} of the solar cells employing the high (LMWF = 1%; left column) and low (LMWF = 52%; right column) performing PM6 batches. Operating conditions of interest are highlighted (black crosses: short-circuit; black logenzes: max-power). (c) Experimentally determined recombination current density J_{rec} (squares and circles) and reconstructed recombination current J_{rec} employing the analytical approach described in Section 9.2 (dotted lines). The required fitting parameters are listed in the inset.

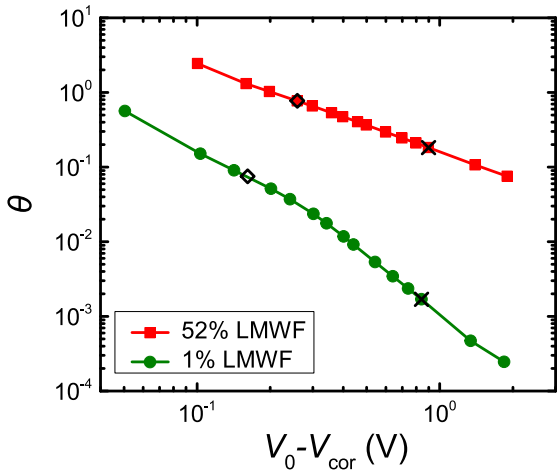

Fig. S27 Comparison of the competition factor $\theta = \tau_{ex}/\tau_{rec}$ of the 1% and 52% LMWF PM6:Y6 blends. Operation conditions of interest are highlighted (black crosses: short-circuit; black lozenges: max-power)

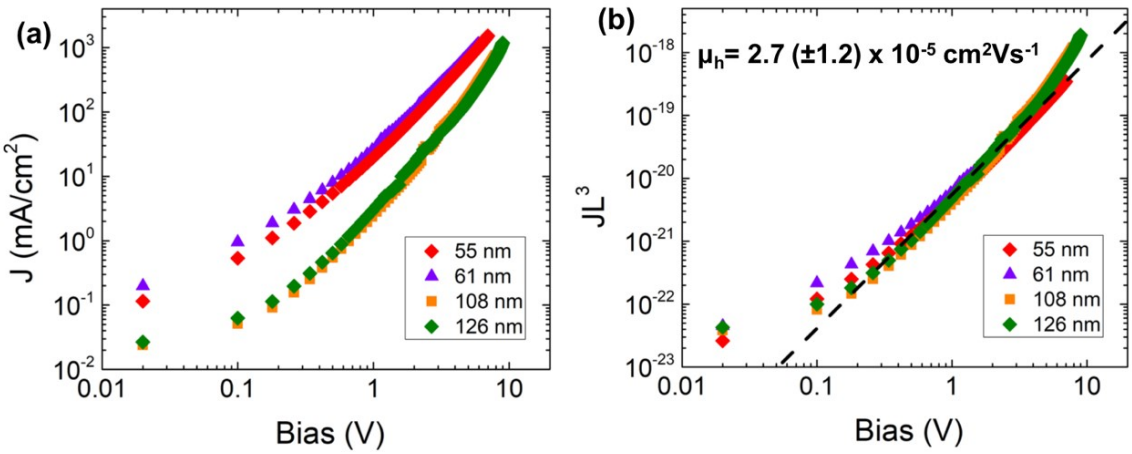

Fig. S28 (a) *J-V* curves of hole-only diodes of the 52% LMWF PM6:Y6 blend at different thicknesses measured in the dark. The current density is multiplied by L^3 showing that the thickness dependence requirement for utilizing the SCLC question is satisfied. The hole-only diodes of the 1% LMWF PM6:Y6 blend is reported in previous literature[7] and found to be an order of magnitude higher than the 52% LMWF blend ($\mu_h = 1.5\ (\pm\ 0.4) \times 10^{-4}$ cm^2 Vs^{-1}). It should be noted that when plotting the thickness dependence of electron mobilities in the 1% LMWF as discussed in the previous report[7], we found that the thickness-dependence of current expected in utilizing the SCLC equation no longer holds and therefore we will stay away from making comparisons of the electron mobilities in these blends using this technique.

7.4. Non-geminate Recombination Dynamics

The recombination current density $J_{rec,sum}$ obtained from the *J-V*-curves can be reconstructed by using the following equation:

$$J_{rec,sum} = J_{rec,bm} + J_{rec,bulk} + J_{rec,surf} . \quad \text{(S12)}$$

The bimolecular component $J_{rec,bm}$ can be described by the following equation:

$$J_{rec,bm} = qLk_{bm}n^2 = \frac{q^2L}{\varepsilon_0\varepsilon_r}\xi(\mu_n + \mu_p)n^2 , \quad \text{(S13)}$$

where k_{bm} is the bimolecular recombination coefficient, ξ is the reduction factor (also known as Langevin prefactor), n is the charge carrier density, and $\mu_{n,p}$ are the electron and hole mobility, respectively. The effective mobility μ_{eff} was used to replace $\mu_{n/p}$. The following expression describes the bulk trap-assisted contribution $J_{rec,bulk}$:

$$J_{rec,bulk} = qLk_{t,b}n = \frac{q^2L}{\varepsilon_0\varepsilon_r}\mu_n N_{t,b}n , \quad \text{(S14)}$$

where $N_{t,b}$ is the density of deep traps in the bulk, and $k_{t,b}$ is the bulk-trap assisted recombination coefficient. Again, the effective mobility μ_{eff} was used. The surface trap-assisted component $J_{rec,surf}$ can be described in a similar way as $J_{rec,bulk}$, with the addition of a field-dependent term:

$$J_{rec,surf} = qLk_{t,s}(V_{cor})n = \frac{q^2}{\varepsilon_0\varepsilon_r}\frac{\mu_p N_{t,s}n}{\exp\left\{\frac{q(V_{bi}-V_{cor})}{kT}\right\}} , \quad \text{(S15)}$$

where $N_{t,s}$ is the density of surface traps, V_{bi} is the built-in voltage, V_{cor} is the corrected voltage, and $k_{t,s}(V_{cor})$ is the surface-trap assisted recombination coefficient. Again, the effective mobility μ_{eff} was used. A detailed description and derivation of this analytical model can be found in a previous report.[27] Subsequently, it is possible to determine the recombination coefficients as well.

The charge carrier lifetimes τ_{rec} can be calculated, once the recombination coefficients k_{rec} are determined. Fundamentally, the following relationship between the non-geminate recombination rate R_{rec} and the charge carrier density n, lifetime τ_{rec}, and the recombination coefficients k_{rec} needs to be considered:

$$R_{rec} = \frac{n}{\tau_{rec}} = k_{rec}n^{\beta} \Leftrightarrow \tau_{rec} = \left(k_{rec}n^{\beta-1}\right)^{-1} , \quad \text{(S16)}$$

where β is the recombination order (trap-assisted, either surface or bulk: $\beta = 1$; bimolecular: $\beta = 2$). If Equation (S10) and Equation (6) shown in the main manuscript are combined, it is possible to determine the total recombination lifetime τ_{rec}, while also considering the different recombination mechanisms that were introduced in the main manuscript:

$$\tau_{rec} = \left(k_{bm}n + k_{t,b} + k_{t,s}\right)^{-1} . \quad \text{(S17)}$$

All necessary constant parameters, fitting parameters and subsequently determined values are summarized in **Table S4**.

Table S4. Overview and values of constants and variables used in the capacitance spectroscopy analysis and the subsequent investigation of the recombination dynamics for the 1% and 52% LMWFs PM6:Y6 devices.

	PM6:Y6 (1% LMWF)	**PM6:Y6 (52% LMWF)**
A/cm^2	0.22	0.22
L/nm	90 ± 5	75 ± 6
ε_r	2.17	3.86
ω/kHz	50	10
V_{bi}/V	0.8417	0.954
V_0/V	0.8415	0.899
V_{sat}/V	-3	-3
μ_{eff}/(cm^{2}V^{-1}s^{-1})	$9.57 \cdot 10^{-5}$	$5.18 \cdot 10^{-6}$
ξ	0.0019	0.0380
$N_{t,b}$/(cm^{-3})	$< 1 \cdot 10^{10}$	$3.13 \cdot 10^{15}$
$N_{t,s}$/(cm^{-2})	$2.72 \cdot 10^{10}$	$8.56 \cdot 10^{11}$
Adj. R^2	0.98805	0.99448
k_{bm}/(cm^{3}s^{-1})	$3.05 \cdot 10^{-13}$	$1.85 \cdot 10^{-13}$
$k_{t,b}$/(s^{-1})	0.08	7598.97

8. References

1 L. A. A. Pettersson, L. S. Roman and O. Inganäs, *J. Appl. Phys.*, 1999, **86**, 487–496.
2 C.-W. Chen, S.-Y. Hsiao, C.-Y. Chen, H.-W. Kang, Z.-Y. Huang and H.-W. Lin, *J. Mater. Chem. A*, 2015, **3**, 9152–9159.
3 A. D. Rakić, *Appl. Opt.*, 1995, **34**, 4755–4767.
4 G. F. Burkhard, E. T. Hoke and M. D. McGehee, *Adv. Mater.*, 2010, **22**, 3293–3297.
5 E. Gann, A. T. Young, B. A. Collins, H. Yan, J. Nasiatka, H. A. Padmore, H. Ade, A. Hexemer and C. Wang, *Rev. Sci. Instrum.*, 2012, **83**, 045110.
6 F. D. Eisner, M. Azzouzi, Z. Fei, X. Hou, T. D. Anthopoulos, T. J. S. Dennis, M. Heeney and J. Nelson, *J. Am. Chem. Soc.*, 2019, **141**, 6362–6374.
7 A. Karki, J. Vollbrecht, A. L. Dixon, N. Schopp, M. Schrock, G. N. M. Reddy and T.-Q. Nguyen, *Adv. Mater.*, 2019, **31**, 1903868.
8 D. Qian, Z. Zheng, H. Yao, W. Tress, T. R. Hopper, S. Chen, S. Li, J. Liu, S. Chen, J. Zhang, X.-K. Liu, B. Gao, L. Ouyang, Y. Jin, G. Pozina, I. A. Buyanova, W. M. Chen, O. Inganäs, V. Coropceanu, J.-L. Bredas, H. Yan, J. Hou, F. Zhang, A. A. Bakulin and F. Gao, *Nat. Mater.*, 2018, **17**, 703.
9 A. Karki, J. Vollbrecht, A. J. Gillett, P. Selter, J. Lee, Z. Peng, N. Schopp, A. L. Dixon, M. Schrock, V. Nadáždy, F. Schauer, H. Ade, B. F. Chmelka, G. C. Bazan, R. H. Friend and T.-Q. Nguyen, *Adv. Energy Mater.*
10 K. Vandewal, K. Tvingstedt, A. Gadisa, O. Inganäs and J. V. Manca, *Phys. Rev. B*, 2010, **81**, 125204.
11 N. A. Ran, J. A. Love, C. J. Takacs, A. Sadhanala, J. K. Beavers, S. D. Collins, Y. Huang, M. Wang, R. H. Friend, G. C. Bazan and T.-Q. Nguyen, *Adv. Mater.*, 2016, **28**, 1482–1488.
12 K. Kawashima, Y. Tamai, H. Ohkita, I. Osaka and K. Takimiya, *Nat. Commun.*, , DOI:10.1038/ncomms10085.
13 S. M. Menke, A. Sadhanala, M. Nikolka, N. A. Ran, M. K. Ravva, S. Abdel-Azeim, H. L. Stern, M. Wang, H. Sirringhaus, T.-Q. Nguyen, J.-L. Brédas, G. C. Bazan and R. H. Friend, *ACS Nano*, 2016, **10**, 10736–10744.
14 D. Baran, T. Kirchartz, S. Wheeler, S. Dimitrov, M. Abdelsamie, J. Gorman, R. S. Ashraf, S. Holliday, A. Wadsworth, N. Gasparini, P. Kaienburg, H. Yan, A. Amassian, C. J. Brabec, J. R. Durrant and I. McCulloch, *Energy Environ. Sci.*, 2016, **9**, 3783–3793.
15 J. Liu, S. Chen, D. Qian, B. Gautam, G. Yang, J. Zhao, J. Bergqvist, F. Zhang, W. Ma, H. Ade, O. Inganäs, K. Gundogdu, F. Gao and H. Yan, *Nat. Energy*, 2016, **1**, 16089.
16 S. M. Tuladhar, M. Azzouzi, F. Delval, J. Yao, A. A. Y. Guilbert, T. Kirchartz, N. F. Montcada, R. Dominguez, F. Langa, E. Palomares and J. Nelson, *ACS Energy Lett.*, 2016, **1**, 302–308.
17 N. A. Ran, S. Roland, J. A. Love, V. Savikhin, C. J. Takacs, Y.-T. Fu, H. Li, V. Coropceanu, X. Liu, J.-L. Brédas, G. C. Bazan, M. F. Toney, D. Neher and T.-Q. Nguyen, *Nat. Commun.*, 2017, **8**, 79.
18 K. D. Rosenthal, M. P. Hughes, B. R. Luginbuhl, N. A. Ran, A. Karki, S.-J. Ko, H. Hu, M. Wang, H. Ade and T.-Q. Nguyen, *Adv. Energy Mater.*, **0**, 1901077.
19 U. Rau, *Phys. Rev. B*, 2007, **76**, 085303.
20 K. D. Rosenthal, M. P. Hughes, B. R. Luginbuhl, N. A. Ran, A. Karki, S.-J. Ko, H. Hu, M. Wang, H. Ade and T.-Q. Nguyen, *Adv. Energy Mater.*, 2019, **9**, 1901077.
21 M. Babics, T. Duan, A. H. Balawi, R.-Z. Liang, F. Cruciani, I.-D. Carja, D. Gottlieb, I. McCulloch, K. Vandewal, F. Laquai and P. M. Beaujuge, *ACS Appl. Energy Mater.*, 2019, **2**, 2717–2722.

22 T. M. Burke, S. Sweetnam, K. Vandewal and M. D. McGehee, *Adv. Energy Mater.*, 2015, **5**, 1500123.
23 V. C. Nikolis, A. Mischok, B. Siegmund, J. Kublitski, X. Jia, J. Benduhn, U. Hörmann, D. Neher, M. C. Gather, D. Spoltore and K. Vandewal, *Nat. Commun.*, 2019, **10**, 1–8.
24 J. Yuan, Y. Zhang, L. Zhou, G. Zhang, H.-L. Yip, T.-K. Lau, X. Lu, C. Zhu, H. Peng, P. A. Johnson, M. Leclerc, Y. Cao, J. Ulanski, Y. Li and Y. Zou, *Joule*, 2019, **3**, 1140–1151.
25 I. Zonno, H. Zayani, M. Grzeslo, B. Krogmeier and T. Kirchartz, *Phys. Rev. Appl.*, 2019, **11**, 054024.
26 S. Albrecht, J. R. Tumbleston, S. Janietz, I. Dumsch, S. Allard, U. Scherf, H. Ade and D. Neher, *J. Phys. Chem. Lett.*, 2014, **5**, 1131–1138.
27 J. Vollbrecht, V. V. Brus, S.-J. Ko, J. Lee, A. Karki, D. X. Cao, K. Cho, G. C. Bazan and T.-Q. Nguyen, *Adv. Energy Mater.*, 2019, **9**, 1901438.